

Classical quantum friction at water–carbon interfaces

Anna T. Bui,¹ Fabian L. Thiemann,^{2,1,3} Angelos Michaelides,¹ and Stephen J. Cox^{1, a)}

¹⁾ Yusuf Hamied Department of Chemistry, University of Cambridge, Lensfield Road, Cambridge, CB2 1EW, United Kingdom

²⁾ Thomas Young Centre, London Centre for Nanotechnology, and Department of Physics and Astronomy, University College London, Gower Street, London, WC1E 6BT, United Kingdom

³⁾ Department of Chemical Engineering, Sargent Centre for Process Systems Engineering, Imperial College London, South Kensington Campus, London, SW7 2AZ, United Kingdom

(Dated: October 26, 2022)

Friction at water–carbon interfaces remains a major puzzle with theories and simulations unable to explain experimental trends in nanoscale waterflow. A recent theoretical framework—quantum friction (QF)—proposes to resolve these experimental observations through nonadiabatic coupling between dielectric fluctuations in water and graphitic surfaces. Here, using a classical model that enables fine-tuning of the solid’s power spectrum, we provide evidence from simulations in general support of QF. In particular, as the principal peak in the solid’s power spectrum begins to overlap with water’s Debye and librational modes, we find an increase in friction comparable to that proposed by QF. At the microscopic level, we find that this contribution to friction manifests more distinctly in the dynamics of the solid’s charge density than that of water. Our results advocate for experimental verification of QF by probing the carbon substrate’s electronic response, rather than water’s structure or dynamics.

Recent advances in nanofluidics^{1,2} show great promise for membrane-based desalination technologies^{3–5} and energy harvesting applications.^{6–11} Owing to the relative ease of fabricating carbon-based nanostructures, a feature common to many of these technologies is the presence of extended interfaces between liquid water and carbon. Despite significant research effort, there are still major gaps^{12–15} in our understanding of water at graphitic surfaces.

Of particular curiosity, experiments have found that friction of water on carbon surfaces is ultra-low compared to other two-dimensional materials.^{16–20} In addition, friction of water is much higher on multilayer graphite^{21–23} than monolayer graphene²⁴ and a peculiar radius dependence in multi-walled carbon nanotubes^{25,26} is also observed. Reproducing these observations has so far remained beyond the realms of molecular simulations,^{27–30} even with the use of highly accurate interatomic potentials.³¹ Consequently, these observations cannot be explained by the traditional “surface roughness” approach^{32,33} that underpins much of our understanding of friction at liquid–solid interfaces.

A recent theoretical study³⁴ by Kavokine *et al.* has sought to explain the differences in friction at graphene vs. graphite by accounting for coupling between collective charge excitations of the liquid and the dynamics of electrons in the carbon substrate. In this framework of “quantum friction” (QF), friction of water on graphite is argued to be larger than that on graphene due to the presence of a dispersionless surface plasmon mode in graphite^{35–37} that overlaps with liquid water’s terahertz (THz) dielectric fluctuations.^{38–40} The purpose of the present article is to explore QF with molecular simulations.

Such coupling between electronic motion in the solid and charge density fluctuations in the liquid is an effect beyond the Born–Oppenheimer approximation.⁴¹ While simulation schemes to account for such nonadiabatic dynamics (“electronic friction”) exist,^{42–44} they rely on the accurate construction of a $(3N \times 3N)$ friction tensor, where N is the total number of atoms explicitly considered in the dynamics. So far, their application has been limited to single gas-phase molecules on metal surfaces,^{45–48} where the friction coefficient on each atom can be well-approximated to depend only on the solid electron density locally.^{49,50} The low-frequency dielectric modes of water, which are essential to the description of QF, however, are inherently collective in nature, prohibiting the application of these sophisticated methods at present.

While accurately accounting for nonadiabatic electronic motion is computationally challenging, low-frequency dielectric response of water is reasonably well captured by simple point charge models.^{51,52} In this article, we therefore focus on this aspect of QF—that dissipative friction forces are mediated through a complex interplay of charge density fluctuations—which is more amenable to classical molecular dynamics (MD) simulations. By extending a standard treatment for polarizability in graphene such that its dielectric fluctuations can be precisely controlled, we will show that coupling between charge density fluctuations in the solid and liquid increases friction in a comparable manner to that predicted by QF. Also similar to QF, this additional contribution is distinct from the typical surface roughness picture for friction. The insights afforded by our simulations suggest that microscopic signatures of QF manifest more distinctly in the dynamics of the solid’s dielectric fluctuations rather than in the structure or dynamics of liquid water.

Model of the liquid–solid interface. The sys-

^{a)} Electronic mail: sjc236@cam.ac.uk

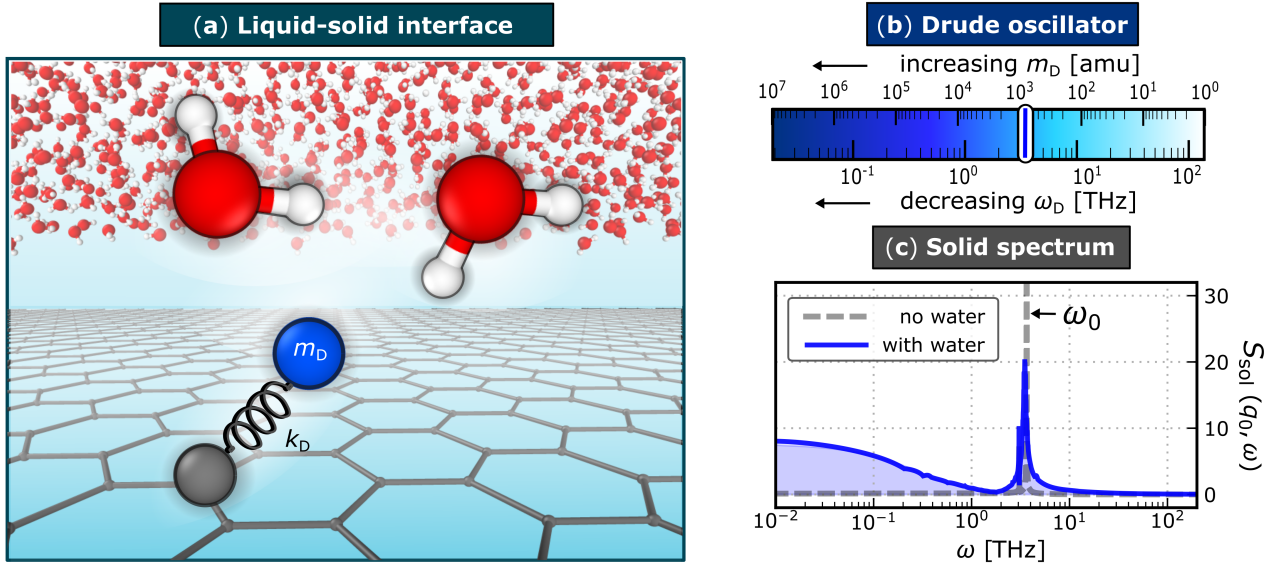


Figure 1. **Model of the liquid–solid interface.** (a) Schematic illustrating the interface of a film of water on a graphene sheet. The graphene’s charge density is described by a classical Drude oscillator model: each C atom carries a charge $+Q_D$ and is attached to a fictitious Drude particle of mass m_D and charge $-Q_D$ via a harmonic spring with force constant k_D . O, H, C atoms and Drude particles are in red, white, grey and blue, respectively. For clarity, only one Drude particle is shown and its displacement from the C atom is exaggerated (see SI for the actual distribution). The characteristic frequency of the Drude oscillators, ω_D is controlled by varying m_D , as indicated by the colorbar in (b). (c) In the absence of water, the power spectrum of the solid, $S_{\text{sol}}(q_0, \omega)$ (shown for $m_D = 10^3$ u), is dominated by a peak at $\omega_0 \approx 3.5$ THz $\gtrsim \omega_D$ indicating a weak coupling between Drude oscillators. With water present, this peak is broadened.

tem we consider consists of a thin film of liquid water on a frozen flat graphene sheet, as shown schematically in Fig. 1(a). To model water, we use the SPC/E model,⁵³ which reasonably captures both the librational modes (hindered molecular rotations) as a sharp peak at $\omega_{\text{lib}} \approx 20$ THz, and the Debye modes (hindered molecular translations) as a broad feature spanning $\sim 10^{-2} - 10^1$ THz.^{51,52} Water–carbon interactions are modeled with a Lennard-Jones potential that reproduces the contact angle of water droplets on graphitic surfaces,⁵⁴ while such a potential captures the essential features of surface roughness contributions to friction, it lacks any dielectric response. For each carbon center we therefore also ascribe a charge $+Q_D$, and attach to it, with a harmonic spring with force constant k_D , a “Drude particle” of mass m_D and charge $-Q_D$. This classical Drude oscillator model is a common approach for modeling electronic polarizability,⁵⁵ and introduces electrostatic interactions between both the water film and the substrate, and the substrate with itself. In the absence of water, the graphene sheet can be considered a set of weakly interacting harmonic oscillators (see SI).

To parameterize the Drude model, we set $Q_D = 1.852 e$ and $k_D = 4184 \text{ kJ mol}^{-1} \text{ \AA}^{-2}$, which have been shown to recover the polarizability tensor of a periodic graphene lattice.⁵⁶ In usual treatments of electronic polarizability, one follows a Car–Parrinello-like scheme⁵⁷ whereby m_D is chosen to be sufficiently small to ensure adiabatic separation of the Drude and nuclear (in this case, water)

motions. Here, we are inspired by the fact that, even for bulk systems, increasing m_D leads to nuclear motion experiencing drag forces.⁵⁸ We therefore treat m_D as a free parameter that tunes the frequency $\omega_D = (k_D/m_D)^{1/2}$ of an individual oscillator, anticipating that this may lead to an increase in friction at the liquid–solid interface. However, the details of how friction may vary with ω_D are not *a priori* obvious. In practice, we choose $1 \lesssim m_D/\text{amu} \lesssim 10^7$, such that $10^{-2} \lesssim \omega_D/\text{THz} \lesssim 10^2$ as indicated in Fig. 1(b). Importantly, changing m_D in this manner does not affect the system’s static equilibrium properties.

In QF, significant overlap between the substrate and liquid water is due to a dispersionless plasmon mode that is present in graphite, but not graphene. While we cannot reasonably expect the simple Drude model to faithfully describe this plasmonic behavior, we can ask a more general question concerning how friction is affected when the substrate and fluid spectra overlap significantly. This question can readily be addressed by tuning m_D , as we describe above, without the need to introduce multilayer graphite. For simplicity, and ease of comparison between systems, we therefore employ a single graphene sheet in all of our simulations.

Overall, our model describes two fluctuating charge densities, $n_{\text{wat}}(\mathbf{r}, t)$ of the water and $n_{\text{sol}}(\mathbf{r}, t)$ of the solid, originating from the collective motion of water molecules and Drude oscillators, respectively, at position \mathbf{r} and time t . The total charges of both the water and the solid are

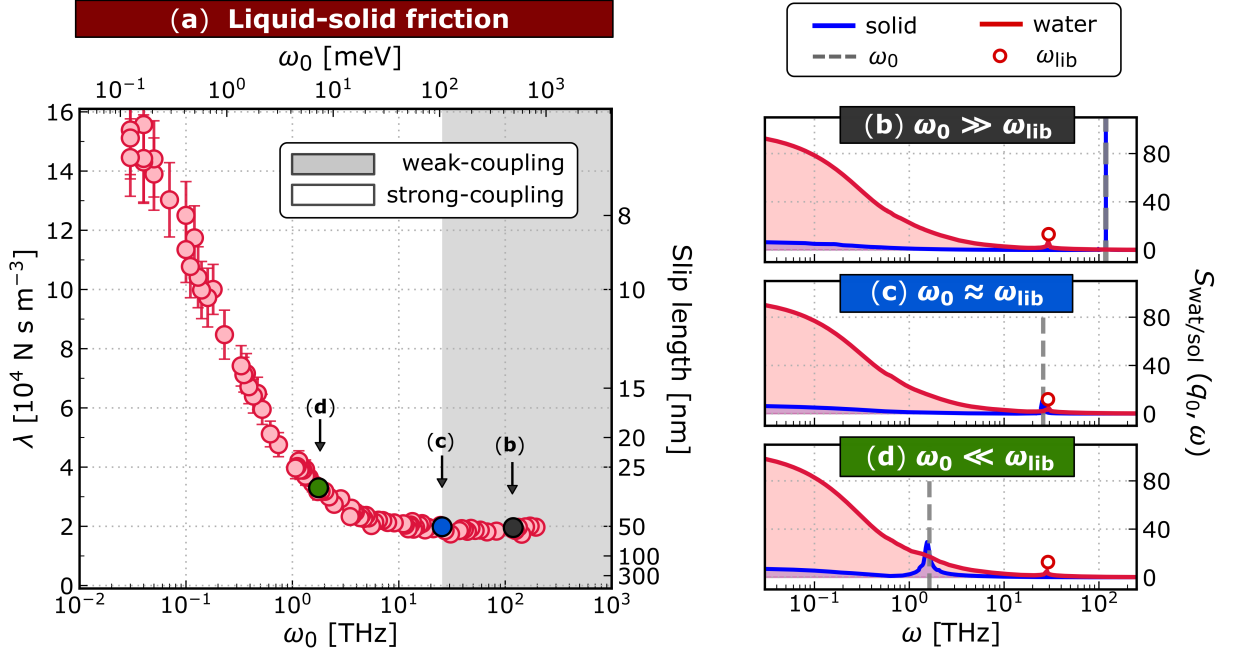


Figure 2. **Friction increases as dielectric fluctuations come into overlap.** (a) The liquid–solid friction coefficient λ is shown against ω_0 . The slip length is given as $b = \eta/\lambda$ where η is the viscosity of water. Statistical errors are obtained from block-averaging. Two regimes are indicated: weak-coupling (shaded gray) where λ remains roughly constant; and strong-coupling (not shaded) where λ increases with decreasing ω_0 . In (b–d), $S_{\text{wat}}(q_0, t)$ and $S_{\text{sol}}(q_0, t)$ are shown for three representative cases $\omega_0 \gg \omega_{\text{lib}}$, $\omega_0 \approx \omega_{\text{lib}}$ and $\omega_0 \ll \omega_{\text{lib}}$, respectively. We see that the increase in λ coincides with $\omega_0 \lesssim \omega_{\text{lib}} \approx 20 \text{ THz}$. The boundary between the regimes is approximate.

strictly conserved. It will be convenient to characterize these charge distributions by their power spectra, e.g., for water,

$$S_{\text{wat}}(q, \omega) = \int_{-\infty}^{\infty} dt \sum_{\alpha, \beta \in \text{wat}} \langle Q_{\alpha} Q_{\beta} e^{-i\mathbf{q} \cdot (\mathbf{x}_{\beta}(t) - \mathbf{x}_{\alpha}(0))} \rangle e^{i\omega t},$$

where Q_{α} is the charge on atom α , whose position in the plane of the graphene sheet at time t is $\mathbf{x}_{\alpha}(t)$, and \mathbf{q} is a wavevector parallel to the graphene sheet. We implicitly only consider the zero wavevector in the direction normal to the graphene sheet. The power spectrum of the solid, $S_{\text{sol}}(q, \omega)$, is similarly defined.

In Fig. 1(c), we present $S_{\text{sol}}(q_0, \omega)$ for $m_D = 10^3 \text{ u}$ both in the absence and presence of water, where $q_0 = 2\pi/L_x \approx 0.25 \text{ \AA}^{-1}$ corresponds to a low wavevector accessible in our simulation box. In the absence of water, $S_{\text{sol}}(q_0, \omega)$ exhibits a single peak at $\omega_0 \approx \omega_D$, confirming it is appropriate to consider the graphene sheet as a set of weakly coupled harmonic oscillators (see SI). In the presence of water, we see the emergence of a broad feature at low frequencies and a broadening of the peak at ω_0 . We will discuss the implication of these observations in the context of friction below. Further technical details of the model, simulation setup, precise definitions of computed quantities and additional tests for the sensitivity of our results are given in the SI.

Friction at the water–carbon interface depends sensitively on ω_0 . We proceed to explore how the fea-

tures of $S_{\text{sol}}(q_0, \omega)$ affect friction at the interface. For each value of m_D , we perform equilibrium MD simulations to extract the liquid–solid friction coefficient λ from the well-established Green–Kubo relationship:^{32,59}

$$\lambda = \frac{1}{\mathcal{A} k_B T} \int_0^{\infty} d\tau \langle \mathcal{F}(0) \cdot \mathcal{F}(\tau) \rangle, \quad (1)$$

where \mathcal{A} is the interfacial lateral area, $\mathcal{F}(\tau)$ is the total force acting on the liquid along a cartesian direction lateral to the graphene sheet at time τ , k_B is Boltzmann’s constant, T is the temperature and $\langle \dots \rangle$ indicates an ensemble average.

In Fig. 2(a), we show the dependence of λ on ω_0 in the range $10^{-2} - 10^2 \text{ THz}$ from a total of 97 simulations. Overall, as ω_0 decreases, λ stays constant until $\omega_0 \approx \omega_{\text{lib}} \approx 20 \text{ THz}$, whereupon further decreasing ω_0 leads to a significant increase in λ . To rationalize this observation, we inspect $S_{\text{wat}}(q_0, \omega)$ and $S_{\text{sol}}(q_0, \omega)$, as shown in Figs. 2(b–d), for three representative cases. Using a feature from each spectrum, ω_0 for the dominant solid peak and ω_{lib} for the water libration, we separate the liquid–solid frictional response into two regimes:

- (i) **Weak-coupling regime:** When $\omega_0 \gtrsim \omega_{\text{lib}}$, the friction coefficient remains roughly constant at $\lambda \approx 1.9 \times 10^4 \text{ N s m}^{-3}$. This value agrees well with previous simulations of water on graphitic surfaces.^{27,31,60–63} In this regime, there is a large

separation of timescales between the dielectric modes of water and the substrate. As a result, there is little overlap between the main peak of $S_{\text{sol}}(q_0, \omega)$ at ω_0 , as seen in Fig. 2(b), and the water dynamics are largely unaffected by varying ω_0 . The motions of the Drude oscillators and the water are not strongly coupled.

- (ii) Strong-coupling regime: When $\omega_0 \lesssim \omega_{\text{lib}}$, hydrodynamic friction increases as ω_0 decreases, reaching $\lambda \approx 15 \times 10^4 \text{ N s m}^{-3}$ for $\omega_0 \approx 0.03 \text{ THz}$. This change in friction of just over one order of magnitude would lead to a significant change in the corresponding slip length from $\sim 60 \text{ nm}$ to $\sim 7 \text{ nm}$. For comparison, experiments have reported water slippage in the range of $0 - 200 \text{ nm}$ on graphene²⁴ and $8 - 13 \text{ nm}$ on graphite.²¹⁻²³ In this regime, there is no longer a large separation in timescales between the Drude oscillators and water’s dielectric modes. Consequently, as seen in Figs. 2(c) and (d), the peak in $S_{\text{sol}}(q_0, \omega)$ at ω_0 now overlaps strongly with water’s librational and Debye modes. The onset of this regime is further supported by the broadening of the main peak in $S_{\text{sol}}(q_0, \omega)$ and the change in the spectrum of the lateral force on the liquid detailed in the SI. We conclude that the increase in friction in this strong-coupling regime is indeed due to coupling of the dielectric modes in the water and the substrate.

To test the sensitivity of this separation into strong- and weak-coupling regimes to the details of the system, we have also performed simulations with different harmonic potentials for the Drude oscillators (see SI). While differences in the absolute values of λ are expected, and indeed observed, the increase of λ for $\omega_0 \lesssim \omega_{\text{lib}}$ is robust.

Comparing molecular simulations with quantum friction theory. Before further analysis, it is useful to make a comparison of our simulation results to QF theory.³⁴ Kavokine *et al.* separated the liquid–solid friction into $\lambda = \lambda_{\text{SR}} + \lambda_{\text{Q}}$, where λ_{SR} is the classical surface roughness contribution and λ_{Q} is the contribution from quantum friction. In our simulations, changing m_{D} does not affect static equilibrium properties such as surface roughness (see SI). In analogy to QF, then, we also decompose the friction coefficient from simulation as $\lambda(\omega_0) = \lambda_{\text{SR}} + \lambda_{\text{THz}}(\omega_0)$, where λ_{THz} originates from the coupling of charge density fluctuations in the THz regime. In practice, we obtain λ_{SR} as the average value of λ in the weak-coupling regime and then obtain λ_{THz} by subtraction.

In Fig. 3(a), we show $\lambda_{\text{THz}}(\omega_0)$ alongside two predictions from Ref. 34, corresponding to different models for graphite’s dispersionless surface plasmon (“1D chain” and “Drude”), giving a QF contribution of $\lambda_{\text{Q}} \approx 0.5 - 1.8 \times 10^4 \text{ N s m}^{-3}$. In the frequency range $2 - 20 \text{ THz}$ where graphite surface plasmons are experimentally observed,³⁵⁻³⁷ we find $\lambda_{\text{THz}} \approx 0.2 - 1.0 \times 10^4 \text{ N s m}^{-3}$. Given the simplicity of our classical model, we are overall

satisfied with the level of agreement between our simulation results and the predictions of QF. In fact, agreement at a quantitative level is found with the “Drude” model for the surface plasmon, which is based on a semi-classical treatment of free electron dynamics.⁶⁴

The microscopic signatures of quantum friction manifest in the solid, not the liquid. A major advantage of performing molecular simulations is the insight they can provide at the microscopic scale. While treating electronic motion as a set of weakly coupled classical Drude oscillators lacks any explicit treatment of quantum mechanical effects, the good agreement between this classical model and QF reinforces the importance of water’s low-frequency dielectric modes in any potential nonadiabatic contributions to friction at water–carbon interfaces.

Going further, we follow Ref. 61 by disentangling the origin of the friction at the interface by reformulating Eq. (1) as $\lambda = \langle \mathcal{F}^2 \rangle \tau_{\text{F}} / (\mathcal{A} k_{\text{B}} T)$, such that the mean-squared force $\langle \mathcal{F}^2 \rangle$ and force decorrelation time τ_{F} quantify static and dynamical components, respectively. As seen in Fig. 3(b), the static component remains essentially constant across the entire range of ω_0 explored in our simulations. An implication of this result is that the water molecules experience the same free energy surface at the interface, an example of which is shown in the inset of Fig. 3(b), independent of ω_0 (see SI). Thus, while the corrugation of the free energy surface (surface roughness) has been widely used to account for the curvature dependence of friction in CNTs^{27,31} and certain differences in hydrodynamic slippage at different materials,^{31,33,60,61,65} it does not describe the physical origins of λ_{THz} . Instead, as seen in Fig. 3(c), the nature of λ_{THz} is entirely dynamical, with the dependence of τ_{F} on ω_0 accounting entirely for the increase in λ_{THz} .

The above analysis strongly suggests that microscopic signatures of nonadiabatic friction manifest in dynamical rather than static properties of the system. We therefore return to the charge densities of the water $\tilde{n}_{\text{wat}}(q_0, t)$ and the solid $\tilde{n}_{\text{sol}}(q_0, t)$ and inspect their autocorrelation functions $C_{\text{wat}}(\tau; q_0)$ and $C_{\text{sol}}(\tau; q_0)$ presented in Figs. 3(d) and 3(e) respectively. While the solid charge density relaxation occurs on a much faster timescale in the strong- than in the weak-coupling regime, the water charge density relaxation barely differs between the two regimes. We have explored other dynamical properties of water, including orientational and hydrogen-bonding relaxation (see SI), and similarly found little effect upon varying ω_0 .

We attribute these contrasting behaviors of the liquid and the solid to the rigidity of water’s hydrogen-bond network, which lacks a clear counterpart from the perspective of the Drude oscillators. In fact, it is even useful to simply compare the relative magnitude of dipoles for a single water molecule μ_{wat} and a Drude oscillator μ_{D} . With our simple point charge model, we have $\langle \mu_{\text{wat}} \rangle = 2.351 \text{ D}$ while $\langle \mu_{\text{D}} \rangle = Q_{\text{D}}(3k_{\text{B}}T/k_{\text{D}})^{1/2} \approx 0.4 \text{ D}$. Thus, while the water molecules only feel the presence of the Drude oscillators as a small perturbation relative to their

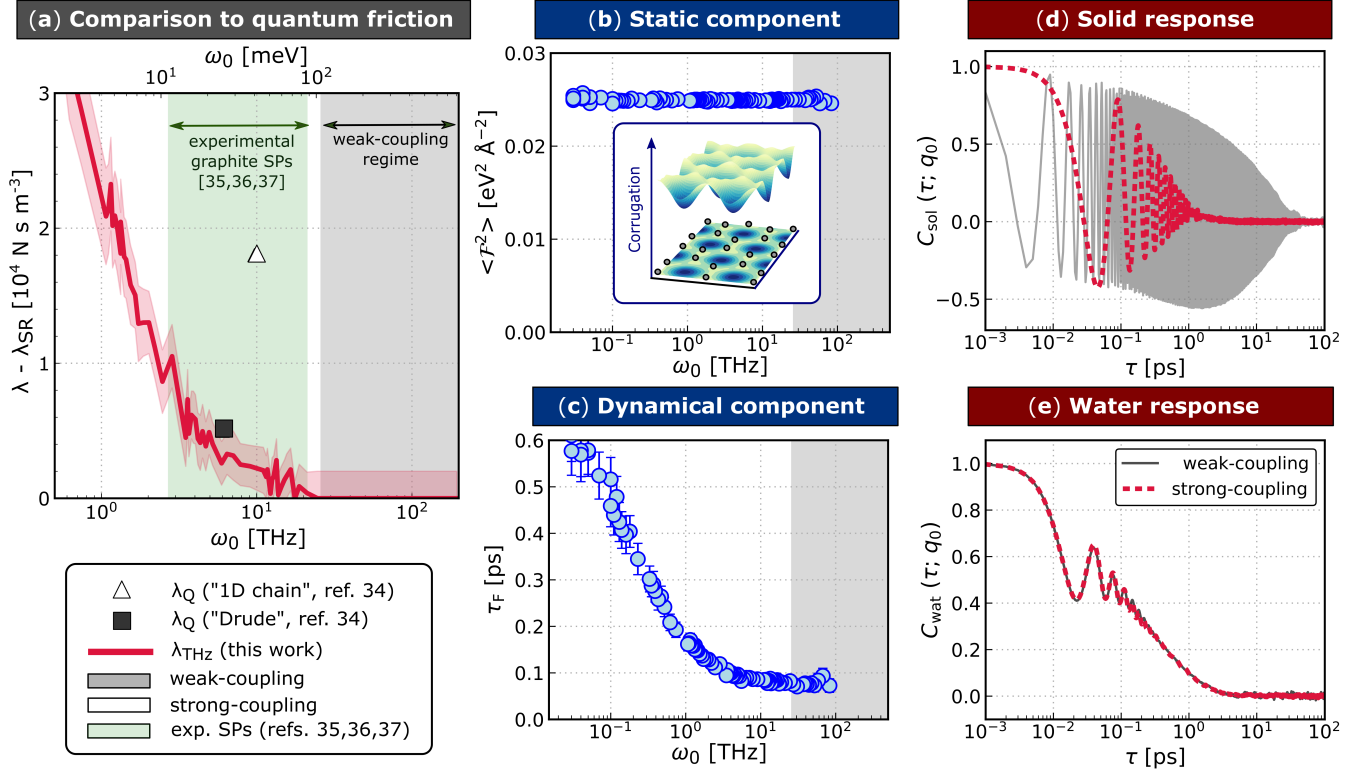


Figure 3. **Microscopic signatures of quantum friction.** (a) $\lambda_{\text{THz}}(\omega_0)$ is comparable to predictions from quantum friction, λ_Q , as indicated in the legend. The shaded red region indicates statistical errors from block-averaging. A range of frequencies for experimental surface plasmons (SPs) in graphite is indicated in green. (b) The static component of the total friction $\langle F^2 \rangle$ is essentially independent of ω_0 and therefore, all liquid–solid interfaces simulated have the same free energy surface shown in the inset (see SI for more details). (c) In contrast, the dynamical component τ_F fully captures the dependence of λ on ω_0 . (d) The charge density correlation functions are shown for representative cases from the weak-coupling ($\omega_0 \approx 100$ THz) and strong-coupling ($\omega_0 \approx 10$ THz) regimes. $C_{\text{sol}}(\tau; q_0)$ decays much more quickly in the strong-coupling regime. (e) In contrast, $C_{\text{wat}}(\tau; q_0)$ is barely affected by changes to ω_0 . The legend in panel (e) also applies to panel (d).

intermolecular interactions, the Drude oscillators feel the impact of the water molecules much more strongly. We speculate that this conclusion also applies to cases where electronic degrees of freedom have been accurately accounted for.

In summary, by using a simple model of charge density fluctuations in a carbon substrate in which we can finely tune the power spectrum, we find increases in interfacial friction comparable to those suggested by a recent theory of quantum friction. We see that the friction increases once the principal peak in the substrate’s power spectrum overlaps with features in water’s power spectrum arising from librational and Debye modes. We show that this extra contribution to the friction is entirely dynamical in its origin, with static equilibrium properties apparently indifferent to the degree of coupling between the water and the substrate. The insights provided by our molecular simulations reveal that the increase in friction manifests at the microscopic scale as a pronounced change in the relaxation of the substrate’s dielectric modes, with little discernible impact on the behavior of water.

Our model, while able to provide a proof of concept

for QF, does not aim to be a rigorous description of water on graphite. We have considered a static graphene sheet, which precludes any role that phonon modes might play.^{66–70} Any changes in surface roughness upon changing from single to multilayer systems have also not been accounted for. Going forwards, it will be essential to explore how these factors affect both the surface roughness and charge density coupling contributions to friction. Advances in simulations of nonadiabatic effects^{43,71,72} to accurately describe the solid electronic excitations in response to collective fluctuations in the liquid will also be a welcome development.

Despite its simplifications, our model captures the increase in the interfacial friction when there is an overlap in the dielectric spectra of the liquid and the solid. It is important to stress that this principle can be generalized to the interfaces of any combination of polar liquid and solid. Since the THz densities of state of a liquid can be reasonably described in simulations, our model opens up the possibility to predict whether different liquids^{73,74} also show a significant QF component. In addition to providing early evidence from simulations in general sup-

port of QF theory, our results suggest a potentially useful strategy for experimental verification. Specifically, the apparent asymmetry between the impact on water and the substrate suggests it may be advantageous to focus experimental efforts on spectroscopies that probe the substrate's electronic response,⁷⁵ rather than seeking hallmarks in the structure or dynamics of the liquid.

ACKNOWLEDGMENTS

This work was performed using resources provided by the Cambridge Service for Data Driven Discovery (CSD3) operated by the University of Cambridge Research Computing Service (www.csd3.cam.ac.uk), provided by Dell EMC and Intel using Tier-2 funding from the Engineering and Physical Sciences Research Council (capital grant EP/T022159/1), and DiRAC funding from the Science and Technology Facilities Council (www.dirac.ac.uk). A.T.B. acknowledges studentship funding from the Ernest Oppenheimer Fund and Peterhouse College, University of Cambridge. S.J.C. is a Royal Society University Research Fellow (Grant No. URF\R1\211144) at the University of Cambridge. For the purpose of open access, the authors have applied a Creative Commons Attribution (CC BY) licence to any Author Accepted Manuscript version arising.

SUPPORTING INFORMATION

The supporting information provides additional details on the results presented in the main article. This includes: the model and simulation details; precise definitions and computational details of the quantities presented in the article; further analysis on the coupling of the liquid and solid charge densities; sensitivity of the results to certain aspects of the simulations and the model and analyses on additional properties of the interface.

DATA AVAILABILITY STATEMENT

The data that supports the findings of this study are openly available at the University of Cambridge Data Repository at <https://doi.org/10.17863/CAM.89536>.

REFERENCES

- L. Bocquet and E. Charlaix, "Nanofluidics, from bulk to interfaces," *Chem. Soc. Rev.* **39**, 1073–1095 (2010).
- L. Bocquet, "Nanofluidics coming of age," *Nature Materials* **19**, 254–256 (2020).
- M. A. Shannon, P. W. Bohn, M. Elimelech, J. G. Georgiadis, B. J. Mariñas, and A. M. Mayes, "Science and technology for water purification in the coming decades," *Nature* **452**, 301–310 (2008).
- M. Elimelech and W. A. Phillip, "The future of seawater desalination: Energy, technology, and the environment," *Science* **333**, 712–717 (2011).
- D. Cohen-Tanugi and J. C. Grossman, "Water desalination across nanoporous graphene," *Nano Letters* **12**, 3602–3608 (2012).
- P. Simon and Y. Gogotsi, "Materials for electrochemical capacitors," *Nature Materials* **7**, 845–854 (2008).
- L. L. Zhang and X. S. Zhao, "Carbon-based materials as supercapacitor electrodes," *Chem. Soc. Rev.* **38**, 2520–2531 (2009).
- B. E. Logan and M. Elimelech, "Membrane-based processes for sustainable power generation using water," *Nature* **488**, 313–319 (2012).
- A. Siria, P. Poncharal, A.-L. Biance, R. Fulcrand, X. Blase, S. T. Purcell, and L. Bocquet, "Giant osmotic energy conversion measured in a single transmembrane boron nitride nanotube," *Nature* **494**, 455–458 (2013).
- H. G. Park and Y. Jung, "Carbon nanofluidics of rapid water transport for energy applications," *Chem. Soc. Rev.* **43**, 565–576 (2014).
- A. Siria, M.-L. Bocquet, and L. Bocquet, "New avenues for the large-scale harvesting of blue energy," *Nature Reviews Chemistry* **1**, 0091 (2017).
- O. Björneholm, M. H. Hansen, A. Hodgson, L.-M. Liu, D. T. Limmer, A. Michaelides, P. Pedevilla, J. Rossmesl, H. Shen, G. Tocci, E. Tyrode, M.-M. Walz, J. Werner, and H. Bluhm, "Water at interfaces," *Chemical Reviews* **116**, 7698–7726 (2016).
- S. Faucher, N. Aluru, M. Z. Bazant, D. Blankshtein, A. H. Brozena, J. Cumings, J. Pedro de Souza, M. Elimelech, R. Epstein, J. T. Fourkas, A. G. Rajan, H. J. Kulik, A. Levy, A. Majumdar, C. Martin, M. McEldrew, R. P. Misra, A. Noy, T. A. Pham, M. Reed, E. Schwegler, Z. Siwy, Y. Wang, and M. Strano, "Critical knowledge gaps in mass transport through single-digit nanopores: A review and perspective," *The Journal of Physical Chemistry C* **123**, 21309–21326 (2019).
- D. Muñoz-Santiburcio and D. Marx, "Confinement-controlled aqueous chemistry within nanometric slit pores," *Chemical Reviews* **121**, 6293–6320 (2021).
- A. Striolo, A. Michaelides, and L. Joly, "The carbon–water interface: Modeling challenges and opportunities for the water–energy nexus," *Annual Review of Chemical and Biomolecular Engineering* **7**, 533–556 (2016).
- J. K. Holt, H. G. Park, Y. Wang, M. Stadermann, A. B. Artyukhin, C. P. Grigoropoulos, A. Noy, and O. Bakajin, "Fast mass transport through sub-2-nanometer carbon nanotubes," *Science* **312**, 1034–1037 (2006).
- M. Whitby, L. Cagnon, M. Thanou, and N. Quirke, "Enhanced fluid flow through nanoscale carbon pipes," *Nano Letters* **8**, 2632–2637 (2008).
- X. Qin, Q. Yuan, Y. Zhao, S. Xie, and Z. Liu, "Measurement of the rate of water translocation through carbon nanotubes," *Nano Letters* **11**, 2173–2177 (2011).
- R. H. Tunuguntla, R. Y. Henley, Y.-C. Yao, T. A. Pham, M. Wannenun, and A. Noy, "Enhanced water permeability and tunable ion selectivity in subnanometer carbon nanotube porins," *Science* **357**, 792–796 (2017).
- A. Keerthi, S. Goutham, Y. You, P. Iamprasertkun, R. A. W. Dryfe, A. K. Geim, and B. Radha, "Water friction in nanofluidic channels made from two-dimensional crystals," *Nature Communications* **12**, 3092 (2021).
- A. Maali, T. Cohen-Bouhacina, and H. Kellay, "Measurement of the slip length of water flow on graphite surface," *Applied Physics Letters* **92**, 053101 (2008).
- D. Ortiz-Young, H.-C. Chiu, S. Kim, K. Voitchovsky, and E. Riedo, "The interplay between apparent viscosity and wettability in nanoconfined water," *Nature Communications* **4**, 2482 (2013).
- S. Li, Q. Li, R. W. Carpick, P. Gumbsch, X. Z. Liu, X. Ding, J. Sun, and J. Li, "The evolving quality of frictional contact with graphene," *Nature* **539**, 541–545 (2016).

- ²⁴Q. Xie, M. A. Alibakhshi, S. Jiao, Z. Xu, M. Hempel, J. Kong, H. G. Park, and C. Duan, "Fast water transport in graphene nanofluidic channels," *Nature Nanotechnology* **13**, 238–245 (2018).
- ²⁵M. Majumder, N. Chopra, R. Andrews, and B. J. Hinds, "Enhanced flow in carbon nanotubes," *Nature* **438**, 44–44 (2005).
- ²⁶E. Secchi, S. Marbach, A. Niguès, D. Stein, A. Siria, and L. Bocquet, "Massive radius-dependent flow slippage in carbon nanotubes," *Nature* **537**, 210–213 (2016).
- ²⁷K. Falk, F. Sedlmeier, L. Joly, R. R. Netz, and L. Bocquet, "Molecular origin of fast water transport in carbon nanotube membranes: Superlubricity versus curvature dependent friction," *Nano Letters* **10**, 4067–4073 (2010).
- ²⁸J. A. Thomas and A. J. H. McGaughey, "Reassessing fast water transport through carbon nanotubes," *Nano Letters* **8**, 2788–2793 (2008).
- ²⁹F. Leoni, C. Calero, and G. Franzese, "Nanoconfined fluids: Uniqueness of water compared to other liquids," *ACS Nano* **15**, 19864–19876 (2021).
- ³⁰G. Cicero, J. C. Grossman, E. Schwegler, F. Gygi, and G. Galli, "Water confined in nanotubes and between graphene sheets: A first principle study," *Journal of the American Chemical Society* **130**, 1871–1878 (2008).
- ³¹F. L. Thiemann, C. Schran, P. Rowe, E. A. Müller, and A. Michaelides, "Water flow in single-wall nanotubes: Oxygen makes it slip, hydrogen makes it stick," *ACS Nano* **16**, 10775–10782 (2022).
- ³²J.-L. Barrat and L. Bocquet, "Influence of wetting properties on hydrodynamic boundary conditions at a fluid/solid interface," *Faraday Discuss.* **112**, 119–128 (1999).
- ³³K. Falk, F. Sedlmeier, L. Joly, R. R. Netz, and L. Bocquet, "Ultra-low liquid/solid friction in carbon nanotubes: Comprehensive theory for alcohols, alkanes, OMCTS, and water," *Langmuir* **28**, 14261–14272 (2012).
- ³⁴N. Kavokine, M.-L. Bocquet, and L. Bocquet, "Fluctuation-induced quantum friction in nanoscale water flows," *Nature* **602**, 84–90 (2022).
- ³⁵M. Portail, M. Carrere, and J. M. Layet, "Dynamical properties of graphite and peculiar behaviour of the low-energy plasmon," *Surface Science* **433–435**, 863–867 (1999).
- ³⁶E. T. Jensen, R. E. Palmer, W. Allison, and J. F. Annett, "Temperature-dependent plasmon frequency and linewidth in a semimetal," *Phys. Rev. Lett.* **66**, 492–495 (1991).
- ³⁷Q. Xing, C. Song, C. Wang, Y. Xie, S. Huang, F. Wang, Y. Lei, X. Yuan, C. Zhang, L. Mu, Y. Huang, F. Xiu, and H. Yan, "Tunable terahertz plasmons in graphite thin films," *Phys. Rev. Lett.* **126**, 147401 (2021).
- ³⁸G. E. Walrafen, "Raman spectrum of water: transverse and longitudinal acoustic modes below 300 cm⁻¹ and optic modes above 300 cm⁻¹," *The Journal of Physical Chemistry* **94**, 2237–2239 (1990).
- ³⁹I. Ohmine and S. Saito, "Water dynamics: Fluctuation, relaxation, and chemical reactions in hydrogen bond network rearrangement," *Accounts of Chemical Research* **32**, 741–749 (1999).
- ⁴⁰M. Heyden, J. Sun, S. Funkner, G. Mathias, H. Forbert, M. Havenith, and D. Marx, "Dissecting the THz spectrum of liquid water from first principles via correlations in time and space," *Proceedings of the National Academy of Sciences* **107**, 12068–12073 (2010).
- ⁴¹M. Born and R. Oppenheimer, "Zur quantentheorie der molekeln," *Annalen der Physik* **389**, 457–484 (1927).
- ⁴²W. Dou and J. E. Subotnik, "Perspective: How to understand electronic friction," *The Journal of Chemical Physics* **148**, 230901 (2018).
- ⁴³M. Head-Gordon and J. C. Tully, "Molecular dynamics with electronic frictions," *The Journal of Chemical Physics* **103**, 10137–10145 (1995).
- ⁴⁴R. Martinazzo and I. Burghardt, "Quantum dynamics with electronic friction," *Phys. Rev. Lett.* **128**, 206002 (2022).
- ⁴⁵M. Askerka, R. J. Maurer, V. S. Batista, and J. C. Tully, "Role of tensorial electronic friction in energy transfer at metal surfaces," *Phys. Rev. Lett.* **116**, 217601 (2016).
- ⁴⁶R. Yin, Y. Zhang, and B. Jiang, "Strong vibrational relaxation of NO scattered from Au(111): Importance of the adiabatic potential energy surface," *The Journal of Physical Chemistry Letters* **10**, 5969–5974 (2019).
- ⁴⁷G. Füchsel, X. Zhou, B. Jiang, J. I. Juaristi, M. Alducin, H. Guo, and G.-J. Kroes, "Reactive and nonreactive scattering of HCl from Au(111): An ab initio molecular dynamics study," *The Journal of Physical Chemistry C* **123**, 2287–2299 (2019).
- ⁴⁸Y. Litman, E. S. Pós, C. L. Box, R. Martinazzo, R. J. Maurer, and M. Rossi, "Dissipative tunneling rates through the incorporation of first-principles electronic friction in instanton rate theory. ii. benchmarks and applications," *The Journal of Chemical Physics* **156**, 194107 (2022).
- ⁴⁹B. Hellsing and M. Persson, "Electronic damping of atomic and molecular vibrations at metal surfaces," *Physica Scripta* **29**, 360–371 (1984).
- ⁵⁰J. I. Juaristi, M. Alducin, R. D. Muiño, H. F. Busnengo, and A. Salin, "Role of electron-hole pair excitations in the dissociative adsorption of diatomic molecules on metal surfaces," *Phys. Rev. Lett.* **100**, 116102 (2008).
- ⁵¹P. Zarzycki and B. Gilbert, "Temperature-dependence of the dielectric relaxation of water using non-polarizable water models," *Physical Chemistry Chemical Physics* **22**, 1011–1018 (2020).
- ⁵²S. Carlson, F. N. Brüning, P. Loche, D. J. Bonthuis, and R. R. Netz, "Exploring the absorption spectrum of simulated water from MHz to infrared," *The Journal of Physical Chemistry A* **124**, 5599–5605 (2020).
- ⁵³H. J. C. Berendsen, J. R. Grigera, and T. P. Straatsma, "The missing term in effective pair potentials," *The Journal of Physical Chemistry* **91**, 6269–6271 (1987).
- ⁵⁴T. Werder, J. H. Walther, R. L. Jaffe, T. Halicioglu, and P. Koumoutsakos, "On the water-carbon interaction for use in molecular dynamics simulations of graphite and carbon nanotubes," *The Journal of Physical Chemistry B* **107**, 1345–1352 (2003).
- ⁵⁵G. Lamoureux and B. Roux, "Modeling induced polarization with classical Drude oscillators: Theory and molecular dynamics simulation algorithm," *The Journal of Chemical Physics* **119**, 3025–3039 (2003).
- ⁵⁶R. P. Misra and D. Blankschtein, "Insights on the role of many-body polarization effects in the wetting of graphitic surfaces by water," *The Journal of Physical Chemistry C* **121**, 28166–28179 (2017).
- ⁵⁷R. Car and M. Parrinello, "Unified approach for molecular dynamics and density-functional theory," *Phys. Rev. Lett.* **55**, 2471–2474 (1985).
- ⁵⁸M. Sprik, "Computer simulation of the dynamics of induced polarization fluctuations in water," *The Journal of Physical Chemistry* **95**, 2283–2291 (1991).
- ⁵⁹L. Bocquet and J.-L. Barrat, "On the Green-Kubo relationship for the liquid-solid friction coefficient," *The Journal of Chemical Physics* **139**, 044704 (2013).
- ⁶⁰G. Tocci, L. Joly, and A. Michaelides, "Friction of water on graphene and hexagonal boron nitride from ab initio methods: Very different slippage despite very similar interface structures," *Nano Letters* **14**, 6872–6877 (2014).
- ⁶¹G. Tocci, M. Bilichenko, L. Joly, and M. Iannuzzi, "Ab initio nanofluidics: disentangling the role of the energy landscape and of density correlations on liquid/solid friction," *Nanoscale* **12**, 10994–11000 (2020).
- ⁶²A. Govind Rajan, M. S. Strano, and D. Blankschtein, "Liquids with lower wettability can exhibit higher friction on hexagonal boron nitride: The intriguing role of solid-liquid electrostatic interactions," *Nano Letters* **19**, 1539–1551 (2019).
- ⁶³A. R. Poggioli and D. T. Limmer, "Distinct chemistries explain decoupling of slip and wettability in atomically smooth aqueous interfaces," *The Journal of Physical Chemistry Letters* **12**, 9060–

- 9067 (2021).
- ⁶⁴J. M. Pitarke, V. M. Silkin, E. V. Chulkov, and P. M. Echenique, “Theory of surface plasmons and surface-plasmon polaritons,” *Reports on Progress in Physics* **70**, 1–87 (2006).
 - ⁶⁵T. A. Ho, D. V. Papavassiliou, L. L. Lee, and A. Striolo, “Liquid water can slip on a hydrophilic surface,” *Proceedings of the National Academy of Sciences* **108**, 16170–16175 (2011).
 - ⁶⁶M. Ma, F. Grey, L. Shen, M. Urbakh, S. Wu, J. Z. Liu, Y. Liu, and Q. Zheng, “Water transport inside carbon nanotubes mediated by phonon-induced oscillating friction,” *Nature Nanotechnology* **10**, 692–695 (2015).
 - ⁶⁷L. Bocquet and R. R. Netz, “Phonon modes for faster flow,” *Nature Nanotechnology* **10**, 657–658 (2015).
 - ⁶⁸E. R. Cruz-Chú, E. Papadopoulou, J. H. Walther, A. Popadić, G. Li, M. Praprotnik, and P. Koumoutsakos, “On phonons and water flow enhancement in carbon nanotubes,” *Nature Nanotechnology* **12**, 1106–1108 (2017).
 - ⁶⁹S. Marbach, D. S. Dean, and L. Bocquet, “Transport and dispersion across wiggling nanopores,” *Nature Physics* **14**, 1108–1113 (2018).
 - ⁷⁰A. Ambrosetti, G. Palermo, and P. L. Silvestrelli, “Quantum-mechanically enhanced water flow in sub-nanometer carbon nanotubes,” (2022), [10.48550/ARXIV.2207.12865](https://arxiv.org/abs/2207.12865).
 - ⁷¹G. Mazzola, A. Zen, and S. Sorella, “Finite-temperature electronic simulations without the born-oppenheimer constraint,” *The Journal of Chemical Physics* **137**, 134112 (2012).
 - ⁷²N. M. Tubman, I. Kylänpää, S. Hammes-Schiffer, and D. M. Ceperley, “Beyond the born-oppenheimer approximation with quantum monte carlo methods,” *Phys. Rev. A* **90**, 042507 (2014).
 - ⁷³P.-A. Cazade, R. Hartkamp, and B. Coasne, “Structure and dynamics of an electrolyte confined in charged nanopores,” *The Journal of Physical Chemistry C* **118**, 5061–5072 (2014).
 - ⁷⁴R. Futamura, T. Iiyama, Y. Takasaki, Y. Gogotsi, M. J. Biggs, M. Salanne, J. Ségolini, P. Simon, and K. Kaneko, “Partial breaking of the coulombic ordering of ionic liquids confined in carbon nanopores,” *Nature Materials* **16**, 1225–1232 (2017).
 - ⁷⁵R. Ulbricht, E. Hendry, J. Shan, T. F. Heinz, and M. Bonn, “Carrier dynamics in semiconductors studied with time-resolved terahertz spectroscopy,” *Rev. Mod. Phys.* **83**, 543–586 (2011).

Supporting information for: Classical quantum friction at water–carbon interfaces

Anna T. Bui,¹ Fabian L. Thiemann,^{2,1,3} Angelos Michaelides,¹ and Stephen J. Cox¹

¹⁾ Yusuf Hamied Department of Chemistry, University of Cambridge, Lensfield Road, Cambridge, CB2 1EW, United Kingdom

²⁾ Thomas Young Centre, London Centre for Nanotechnology, and Department of Physics and Astronomy, University College London, Gower Street, London, WC1E 6BT, United Kingdom

³⁾ Department of Chemical Engineering, Sargent Centre for Process Systems Engineering, Imperial College London, South Kensington Campus, London, SW7 2AZ, United Kingdom

(Dated: October 26, 2022)

This supplementary information provides additional details on the results presented in the main article. This includes: the model and simulation details; precise definitions and computational details of the quantities presented in the article; further analysis on the coupling of the liquid and solid charge densities; sensitivity of the results to certain aspects of the simulations and the model and analyses on additional properties of the interface.

CONTENTS

S1. Classical molecular dynamics simulation details	S2
S1.1. Model description	S2
S1.2. System set-up	S3
S1.3. Simulation details	S4
S2. Computation of properties	S5
S2.1. Friction coefficient	S5
S2.2. Charge density spectra	S5
S2.3. Charge density autocorrelation function	S6
S3. Sensitivity of the friction coefficient	S7
S3.1. Convergence of the Green–Kubo friction coefficient	S7
S3.2. System size	S7
S3.3. Simulation time	S8
S3.4. Time-step	S9
S3.5. Thermostats	S10
S3.6. Liquid film thickness	S11
S3.7. Electrostatic boundary conditions	S11
S4. Coupling of charge densities	S13
S4.1. Charge densities in the absence of water	S13
S4.2. Charge densities in the presence of water	S13
S4.3. Force spectra	S14
S5. Sensitivity of the dependence of friction on solid charge density frequency	S16
S5.1. Varying the Drude charge Q_D	S16
S5.2. Varying the force constant k_D	S17
S6. Additional properties of the interface	S18
S6.1. Static properties	S18
S6.2. Dynamical properties	S19
References	S21

S1. CLASSICAL MOLECULAR DYNAMICS SIMULATION DETAILS

S1.1. Model description

We consider a system of a film of liquid water on a flat graphene sheet as described in the main article. Liquid water can be modeled by rigid simple point charge models with potential energy functions of the form

$$\mathcal{U}_{\text{wat}}(\mathbf{R}_{\text{wat}}^N) = \sum_{i < j}^N u_{\text{LJ}}(|\mathbf{r}_{\text{O},i} - \mathbf{r}_{\text{O},j}|) + \sum_{i < j}^N \sum_{\alpha, \beta} \frac{Q_{\alpha,i} Q_{\beta,j}}{|\mathbf{r}_{\alpha,i} - \mathbf{r}_{\beta,j}|}, \quad (\text{S1})$$

where $\mathbf{R}_{\text{wat}}^N$ denotes the set of atomic positions for a configuration of N water molecules, $\mathbf{r}_{\text{O},i}$ denotes position of the oxygen atom on water molecule i and $Q_{\alpha,i}$ is the charge of site α located at position $\mathbf{r}_{\alpha,i}$. The first set of sums in Eq. S1 captures short-ranged repulsion and non-electrostatic “long-ranged” attraction between water molecules with the usual Lennard-Jones 12-6 potential

$$u_{\text{LJ}}(r) = 4\epsilon \left[\left(\frac{\sigma}{r} \right)^{12} - \left(\frac{\sigma}{r} \right)^6 \right], \quad (\text{S2})$$

which is parameterized by an energy scale ϵ and a length scale σ . The second set of sums in Eq. S1 describes electrostatic interactions. Here, we adopt a unit system for electrostatics in which $4\pi\epsilon_0 = 1$ where ϵ_0 is the permittivity of free space.

In the standard surface roughness picture, the liquid interacts with the solid through long-ranged van der Waals attraction and short-range Pauli repulsion, which we model with a 12-6 Lennard-Jones potential between the oxygen atoms on the water and the carbon atoms in the graphene sheet

$$\mathcal{U}_{\text{SR}}(\mathbf{R}_{\text{wat}}^N, \mathbf{R}_{\text{sol}}^M) = \sum_i^N \sum_j^M u_{\text{LJ}}(|\mathbf{r}_{\text{O},i} - \mathbf{r}_{\text{C},j}|), \quad (\text{S3})$$

where $\mathbf{R}_{\text{sol}}^M$ denotes the set of atomic positions for a configuration of M carbon atoms. Here, for simplicity, we fix the positions of the carbon atoms.

Polarization of the solid can then be incorporated with the classical Drude oscillator model.¹ Each carbon core now carries a positive charge $+Q_{\text{D}}$ and is attached to a Drude particle of charge $-Q_{\text{D}}$ and mass m_{D} through a harmonic spring with force constant k_{D} . The potential energy function of the solid then has the form

$$\mathcal{U}_{\text{sol}}(\mathbf{R}_{\text{sol}}^M) = \sum_i^M \frac{1}{2} k_{\text{D}} |\mathbf{r}_{\text{C},i} - \mathbf{r}_{\text{D},i}|^2 + \sum_{i < j}^M \sum_{\alpha, \beta} \frac{Q_{\alpha,i} Q_{\beta,j}}{|\mathbf{r}_{\alpha,i} - \mathbf{r}_{\beta,j}|} \phi(|\mathbf{r}_{\alpha,i} - \mathbf{r}_{\beta,j}|). \quad (\text{S4})$$

The first set of sums describes the total harmonic interaction of all Drude oscillators in the solid. The second set of sums describes the electrostatic interactions between the oscillators. To avoid the “polarization catastrophe”, a Thole function,² $\phi(r)$, is used to damp Coulomb interactions at short distances. This function has the form

$$\phi(r) = 1 - \left(1 + \frac{sr}{2} \right) e^{-sr}, \quad (\text{S5})$$

where the scaling coefficient s is determined by the polarizability of the carbon atom α_{C} and a Thole damping parameter δ_{C} via $s = \delta_{\text{C}}/(\alpha_{\text{C}})^{1/3}$.

In the absence of a field, each Drude particle oscillates around its core atom position \mathbf{r}_{C} . In an electric field $\mathbf{E}(t)$, here arising from the fluctuating charge density of water, the Drude particle oscillates around $\mathbf{r}_{\text{C}} + \mathbf{d}(t)$ where $\mathbf{d}(t)$ is the displacement of Drude particle from the core atom at time t and is given by $\mathbf{d}(t) = Q_{\text{D}} \mathbf{E}(t)/k_{\text{D}}$. The instantaneous induced dipole from the Drude oscillator is $\boldsymbol{\mu}_{\text{D}}(t) = Q_{\text{D}} \mathbf{d}(t) = Q_{\text{D}}^2 \mathbf{E}(t)/k_{\text{D}}$. The isotropic atomic polarizability is then seen to be^{1,3-5}

$$\alpha_{\text{C}} = \frac{Q_{\text{D}}^2}{k_{\text{D}}}. \quad (\text{S6})$$

The polarization response of the solid is therefore controlled by the parameters Q_{D} and k_{D} .

Introduction of point charges in the solid now introduces electrostatic interactions between the solid and the liquid, which we refer to as the charge density coupling term:

$$\mathcal{U}_{\text{CC}}(\mathbf{R}_{\text{wat}}^N, \mathbf{R}_{\text{sol}}^M) = \sum_i^N \sum_j^M \sum_{\alpha, \beta} \frac{Q_{\alpha, i} Q_{\beta, j}}{|\mathbf{r}_{\alpha, i} - \mathbf{r}_{\beta, j}|}. \quad (\text{S7})$$

The overall potential energy of the system is:

$$\mathcal{U}_{\text{tot}}(\mathbf{R}_{\text{wat}}^N, \mathbf{R}_{\text{sol}}^M) = \mathcal{U}_{\text{wat}}(\mathbf{R}_{\text{wat}}^N) + \mathcal{U}_{\text{SR}}(\mathbf{R}_{\text{wat}}^N, \mathbf{R}_{\text{sol}}^M) + \mathcal{U}_{\text{sol}}(\mathbf{R}_{\text{sol}}^M) + \mathcal{U}_{\text{CC}}(\mathbf{R}_{\text{wat}}^N, \mathbf{R}_{\text{sol}}^M). \quad (\text{S8})$$

We reiterate that in previous work,^{6,7} classical treatments of liquid–solid interfacial friction have focused on the first two terms of the potential. Here, our model considers also interactions between fluctuating charge densities in the liquid and the solid through the addition of the last two terms.

S1.2. System set-up

For the results presented in the main article, the simulations were carried out with 724 water molecules in a thin film of thickness $\approx 37 \text{ \AA}$ above a graphene layer of 240 carbon atoms, as illustrated in Fig. S1. Each carbon atom is attached to one Drude particle so there are 240 Drude particles. The orthorhombic cell has dimension $\approx 26 \times 25 \times 150 \text{ \AA}^3$. In addition, simulations of larger system sizes and of water films with different thicknesses were also performed to check the sensitivity of the results, which are presented in Sec. S3.

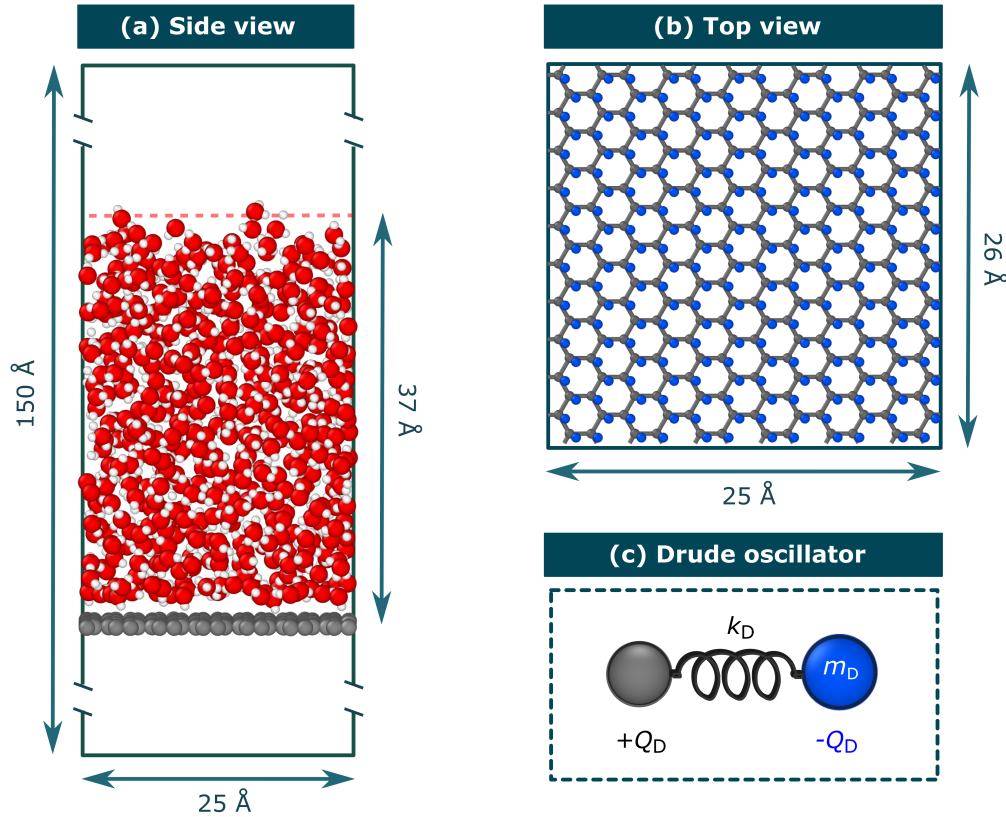


Figure S1. **System set-up.** The view from (a) the side of the liquid–solid interface and (b) the top of the solid sheet. Oxygen, hydrogen, carbon atoms and Drude particles are in red, white, grey and blue, respectively. The dark solid lines represent the edges of the simulation box. (c) The classical Drude oscillator is used to model charge density in the solid, whose parameters include: the harmonic spring constant k_D , the Drude mass m_D , charge on the core carbon atom $+Q_D$ and on the Drude particle $-Q_D$.

S1.3. Simulation details

All simulations were carried out with the LAMMPS simulations package.^{8,9} Water–water interactions were described with the SPC/E water model.¹⁰ The geometry of water molecules was constrained using the RATTLE algorithm.¹¹ The carbon positions of the sheet were fixed. Water–carbon interaction responsible for the surface roughness was modeled with Werder parameters.¹² Charge densities on the graphene sheet were modeled using the classical Drude oscillator model^{1,13} with Thole damping² using parameters from Misra and Blankschtein.¹⁴ The value of parameters for all interaction potentials in the simulations are summarized in Tabs. S1 and S2. All Lennard-Jones interactions were truncated and shifted at 10 Å. Electrostatic interactions were cut off at 10 Å and long-ranged interactions were evaluated using particle–particle particle–mesh Ewald summation¹⁵ such that the RMS error in the forces was a factor of 10^5 smaller than the force between two unit charges separated by a distance of 1.0 Å.¹⁶ Drude mass choices to change the solid charge density frequency are in the range of $1 - 10^7$ amu.

Subsystem	Atom type	Mass [amu]	Charge [e]
water	O	15.9994	−0.8476
	H	1.008	+0.4238
carbon	C	*	+1.8520
	D	$1 - 10^7$	−1.8520

Table S1. **Parameters for masses and charges for atoms in simulations.** Parameters for water are from the SPC/E model¹⁰ and those for the carbon solid are from Misra and Blankschtein.¹⁴ The * denotes that C atoms are fixed so their masses do not contribute to the dynamics. The letter D is used to denote Drude particles.

Interaction potential	Potential form	Parameters
SPC/E ¹⁰	rigid bond	$r_{\text{OH}} = 1.0 \text{ Å}$
	rigid angle	$\theta_{\text{HOH}} = 109.47^\circ$
	Lennard-Jones	$\epsilon_{\text{OO}} = 0.1553 \text{ kcal mol}^{-1}$
		$\sigma_{\text{OO}} = 3.166 \text{ Å}$
Werder ¹²	Lennard-Jones	$\epsilon_{\text{CO}} = 0.1553 \text{ kcal mol}^{-1}$
		$\sigma_{\text{CO}} = 3.190 \text{ Å}$
Misra and Blankschtein ¹⁴	Thole damping ²	$\delta_{\text{C}} = 1.507$
	harmonic bond	$k_{\text{D}} = 1000 \text{ kcal mol}^{-1} \text{ Å}^{-2}$

Table S2. **Parameters for interaction potentials (force fields) employed in simulations.** For polarization in the solid, the choice of k_{D} and Q_{D} from Misra and Blankschtein¹⁴ gives an isotropic polarizability of $\alpha_{\text{C}} = 1.139 \text{ Å}^3$.

The simulations were carried out in the canonical (NVT) ensemble, where the temperature was held at 300 K. Two separate Nosé–Hoover thermostats^{17,18} were applied to the water and Drude particles. Each thermostat is a Nosé–Hoover chain with 10 thermostats and a damping constant of 0.1 ps. Dynamics were propagated using the velocity Verlet algorithm with a time-step of 1 fs, unless specified otherwise. Each system was equilibrated for 100 ps and the subsequent 10 ns was used for analysis to give the results presented in the main article. The sensitivity of the results to different simulation settings is presented in Sec. S3.

S2. COMPUTATION OF PROPERTIES

S2.1. Friction coefficient

For each equilibrium MD simulation, the friction coefficient was evaluated through the Green–Kubo formula¹⁹ involving the time integral of the force autocorrelation function defined as:

$$\lambda_{\text{GK}}(\tau) = \frac{1}{\mathcal{A}k_{\text{B}}T} \int_0^\tau dt \langle \mathcal{F}(0) \cdot \mathcal{F}(t) \rangle, \quad (\text{S9})$$

where \mathcal{A} is the interfacial lateral area, $\langle \cdots \rangle$ indicates an ensemble average and $\mathcal{F}(t)$ denotes the instantaneous lateral force exerted on the liquid by the solid at time t . $\mathcal{F}(t)$ is evaluated as the total summed force acting on all water molecules of a given configuration averaged over both in-plane dimensions (x, y) and is saved at every time-step (1 fs). In principle, the friction coefficient of the system is recovered at the long-time limit:

$$\lambda = \lim_{\tau \rightarrow \infty} \lambda_{\text{GK}}(\tau). \quad (\text{S10})$$

However, at long times, the integral in Eq. S9 decays to zero due to the finite lateral extent of the system^{20,21} so evaluating $\lambda_{\text{GK}}(\tau)$ to a plateau is commonly employed.^{7,22,23} It has been shown that taking the maximum of $\lambda_{\text{GK}}(\tau)$ only recovers friction correctly when there is a separation of timescales between the decay time and the memory time of the force autocorrelation function.²⁴ Since we are probing behaviors of the interface where there is no separation of timescales, we approximate λ as the plateaued friction coefficient averaged between correlation time of 5 – 10 ps. Justification of this choice is detailed in Sec. S3. For each Drude mass, we perform equilibrium MD simulations to extract λ . The error bars correspond to the statistical errors obtained from splitting the entire trajectory into 100 blocks such that each block is 100 ps long.

In the main text, we decompose the static and dynamical components of the friction coefficient by reformulating the Green–Kubo expression in terms of the mean square force $\langle \mathcal{F}^2 \rangle$ and the force decorrelation time τ_{F} :

$$\lambda = \frac{1}{\mathcal{A}k_{\text{B}}T} \langle \mathcal{F}^2 \rangle \tau_{\text{F}}, \quad (\text{S11})$$

where

$$\tau_{\text{F}} = \int_0^\infty dt \frac{\langle \mathcal{F}(0) \cdot \mathcal{F}(t) \rangle}{\langle \mathcal{F}^2 \rangle}. \quad (\text{S12})$$

In practice, we computed the friction coefficient and the mean square force first before obtaining the force decorrelation time via $\tau_{\text{F}} = \lambda \mathcal{A}k_{\text{B}}T / \langle \mathcal{F}^2 \rangle$.

S2.2. Charge density spectra

In the main article, the charge density distribution of the solid and the liquid are characterized by their power spectra defined as

$$S_{\text{sol}}(q, \omega) = \int_{-\infty}^{\infty} dt \sum_{\alpha, \beta \in \text{sol}} \langle Q_{\alpha} Q_{\beta} e^{-i\mathbf{q} \cdot (\mathbf{x}_{\beta}(t) - \mathbf{x}_{\alpha}(0))} \rangle e^{i\omega t}, \quad (\text{S13})$$

$$S_{\text{wat}}(q, \omega) = \int_{-\infty}^{\infty} dt \sum_{\alpha, \beta \in \text{wat}} \langle Q_{\alpha} Q_{\beta} e^{-i\mathbf{q} \cdot (\mathbf{x}_{\beta}(t) - \mathbf{x}_{\alpha}(0))} \rangle e^{i\omega t}, \quad (\text{S14})$$

respectively. Here, Q_{α} is the charge on atom α , whose position in the plane of the graphene sheet at time t is $\mathbf{x}_{\alpha}(t)$, and \mathbf{q} is a wavevector parallel to the graphene sheet. In practice, we computed at every time-step (1 fs) the Fourier components of the charge densities for the solid and the liquid, defined as

$$\tilde{n}_{\text{sol}}(\mathbf{q}, t) = \sum_{\alpha \in \text{sol}} Q_{\alpha} e^{i\mathbf{q} \cdot \mathbf{x}_{\alpha}(t)}, \quad (\text{S15})$$

$$\tilde{n}_{\text{wat}}(\mathbf{q}, t) = \sum_{\alpha \in \text{wat}} Q_{\alpha} e^{i\mathbf{q} \cdot \mathbf{x}_{\alpha}(t)}. \quad (\text{S16})$$

As we are interested in the long-wavelength limit ($q \rightarrow 0$), we implicitly only considered $\mathbf{q} = \mathbf{q}_0$, the lowest wavevector in the x direction accessible in our simulation box, the magnitude of which is $q_0 = 2\pi/L_x \approx 0.25 \text{ \AA}^{-1}$ where L_x is the length of the box in the x direction. The power spectra are, similar to in Eqs. S13 and S14, obtained from taking the Fourier transform of their autocorrelation functions:

$$S_{\text{sol}}(q, \omega) = \int_{-\infty}^{+\infty} dt \langle \tilde{n}_{\text{sol}}(\mathbf{q}, 0) \cdot \tilde{n}_{\text{sol}}^*(\mathbf{q}, t) \rangle e^{i\omega t}, \quad (\text{S17})$$

$$S_{\text{wat}}(q, \omega) = \int_{-\infty}^{+\infty} dt \langle \tilde{n}_{\text{wat}}(\mathbf{q}, 0) \cdot \tilde{n}_{\text{wat}}^*(\mathbf{q}, t) \rangle e^{i\omega t}. \quad (\text{S18})$$

To ensure the spectrum is independent of noise, a Savitzky–Golay filter²⁵ was applied. The resulting spectra without further fitting are presented in the main article.

S2.3. Charge density autocorrelation function

To characterize relaxation of the solid and the liquid charge densities, we computed their respective normalized autocorrelation functions, defined as:

$$C_{\text{sol}}(\tau; q) = \frac{\langle \tilde{n}_{\text{sol}}(\mathbf{q}, 0) \cdot \tilde{n}_{\text{sol}}^*(\mathbf{q}, \tau) \rangle}{\langle |\tilde{n}_{\text{sol}}(\mathbf{q})|^2 \rangle}, \quad (\text{S19})$$

$$C_{\text{wat}}(\tau; q) = \frac{\langle \tilde{n}_{\text{wat}}(\mathbf{q}, 0) \cdot \tilde{n}_{\text{wat}}^*(\mathbf{q}, \tau) \rangle}{\langle |\tilde{n}_{\text{wat}}(\mathbf{q})|^2 \rangle}. \quad (\text{S20})$$

Again, focusing on the long-wavelength limit, we show the results for $C_{\text{sol}}(\tau; q_0)$ and $C_{\text{wat}}(\tau; q_0)$ in the main article.

S3. SENSITIVITY OF THE FRICTION COEFFICIENT

To assess the robustness of our results to the choice of simulation settings, here we present an extensive set of tests on the sensitivity of the friction coefficients computed to certain aspects of our simulations. In these tests, we show the results for two representative cases: $m_D = 1$ amu for the weak-coupling regime and $m_D = 5000$ amu for the strong-coupling regime.

S3.1. Convergence of the Green–Kubo friction coefficient

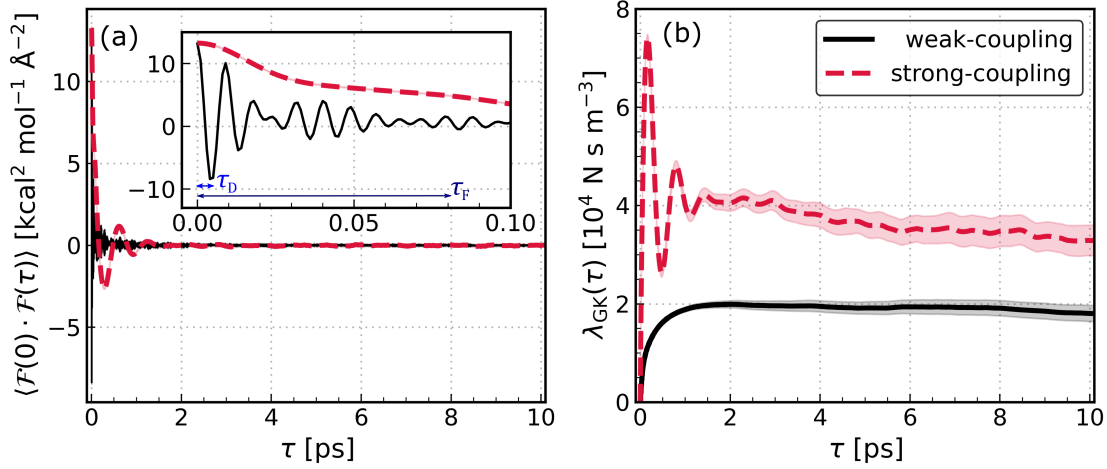


Figure S2. **Convergence of the Green–Kubo friction coefficient** (a) The force autocorrelation function of two representative cases in the weak-coupling and strong-coupling regimes. The inset shows clearer the oscillations due to the Drude dynamics. The memory time τ_D and the decay time τ_F are marked for the weak-coupling case. (b) The convergence of λ_{GK} where statistical errors (shaded area) are obtained from block-averaging.

As seen from Fig. S2, the force autocorrelation $\langle \mathcal{F}(0) \cdot \mathcal{F}(\tau) \rangle$ shows oscillations due to charge density fluctuations in the solid at short timescales before decaying to zero at longer timescales. We can characterize two particular timescales: (i) the time at which the first minimum is reached, $\tau_D \propto \omega_D$, due to motion of the Drude oscillators and (ii) the force decorrelation time, $\tau_F \propto \lambda$, as defined by Eq. S12. These are marked for the weak-coupling case in the inset of Fig. S2(a). In $\lambda_{\text{GK}}(\tau)$, these timescales manifest in a peak at τ_D and a plateau after τ_F . In the weak-coupling regime where the Drude mass is low, there is a separation of timescales as $\tau_D \ll \tau_F$. A decrease in the solid charge density frequency in this regime only increases τ_D but not τ_F . The peak at τ_D is a local maximum, increasing in height as Drude mass increases, and a plateau is observed at times intermediate between τ_D and τ_F , unchanged in height. This is consistent with the converged friction coefficient remaining at $\lambda \approx 1.9 \times 10^4 \text{ N s m}^{-3}$. In the strong-coupling regime where the solid frequency is slow, τ_D is now comparable to τ_F . A decrease in the solid charge density frequency in this regime increases both τ_D and τ_F . As τ_F governs the value of λ_{GK} at long times, the converged friction coefficient now increases with decreasing charge density frequency. In order to get a consistent value for the friction coefficient, it is important to extract λ from $\lambda_{\text{GK}}(\tau)$ at $\tau > \tau_F$. Therefore, taking the maximum of $\lambda_{\text{GK}}(\tau)$ as in some studies^{23,26,27} is not appropriate, as also shown previously by Oga *et al.*²⁴

For simulations with the largest Drude mass $m_D = 10^7$ amu, we observe a plateau in $\lambda_{\text{GK}}(\tau)$ from $\tau \gtrsim 5$ ps. Therefore, we give the converged friction coefficient in all cases to be the average of values of $\lambda_{\text{GK}}(\tau)$ evaluated at correlation time between $5 < \tau/\text{ps} < 10$.

S3.2. System size

To make sure the employed system size is sufficient to obtained converged values, we checked if our results remain consistent at larger system sizes. In Fig. S3, the friction coefficient for two representative Drude masses are shown for systems with different lateral areas in the (x, y) plane. The additional

simulations were carried out on an interface with approximately the same liquid film thickness ≈ 37 Å. The friction coefficients computed from these simulations are almost identical to those presented in the main article.

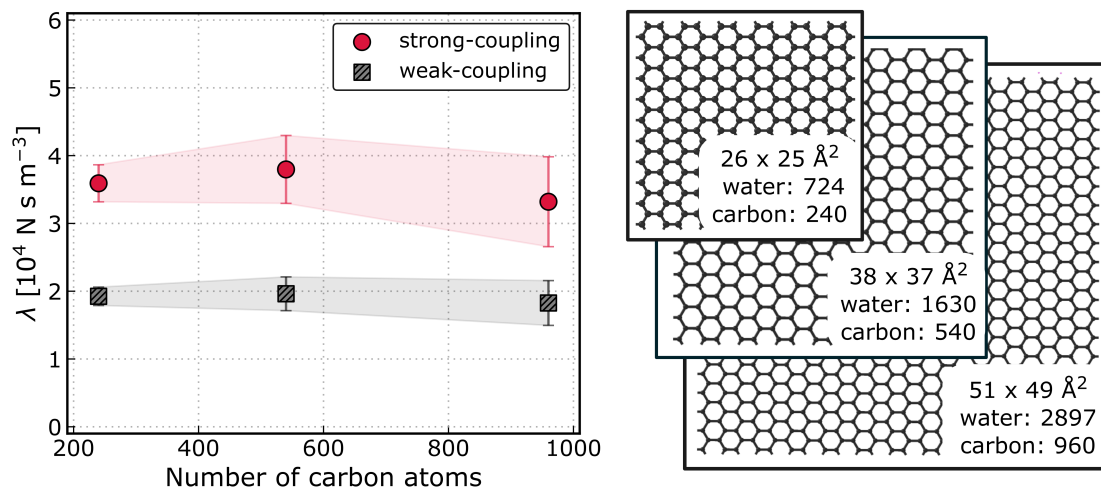


Figure S3. **Sensitivity of friction coefficient to system size.** Statistical errors are obtained from block-averaging. The three system sizes tested are illustrated on the right panel where only the solid sheets are shown. The corresponding total area for the sheet and the number of water molecules and carbon atoms are given for each system

S3.3. Simulation time

Analogous to checking the impact of system size, we checked the convergence of the friction coefficient with the simulation time length, as presented in Fig. S4. For all cases, the friction coefficient is found to change relatively little with increasing simulation time. While statistical errors are larger for shorter simulations, simulation times as short as 1 ns is enough to converge friction to within 10%. Therefore, the employed simulation time of 10 ns is sufficient for a converged friction coefficient.

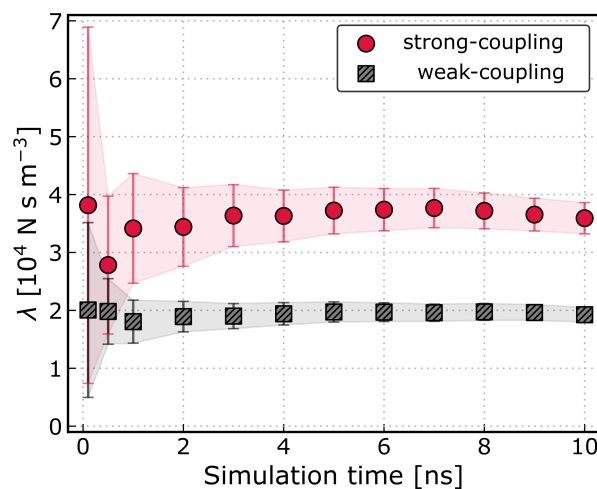


Figure S4. **Sensitivity of friction coefficient to simulation time.** λ changes relatively little with increasing simulation time. Statistical errors are obtained from block-averaging.

S3.4. Time-step

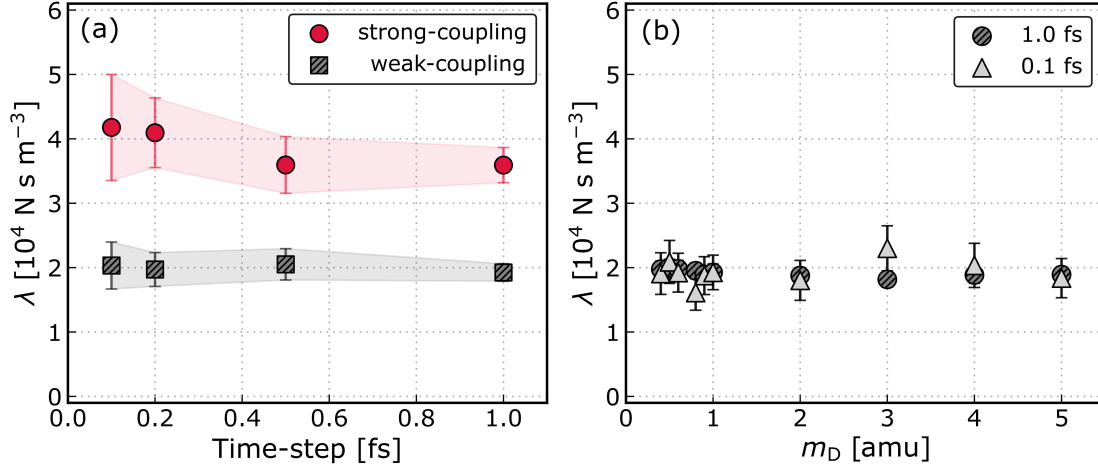


Figure S5. **Sensitivity of friction coefficient to time-step.** (a) Dependence of the computed λ on the time-step used in simulations. (b) Comparison of λ for simulations with $m_D \lesssim 5$ amu using a time-step of 0.1 and 1 fs. Statistical errors are obtained from block-averaging.

We test the sensitivity of the friction coefficients in both the weak-coupling and strong-coupling regimes with the time-step used in simulations and see that the results agree well for time-step of 0.1, 0.2, 0.5 and 1 fs, as shown in Fig. S5(a). However, when dealing with small Drude masses, problems with energy drifts often arise due to the inherently high frequency of the individual Drude oscillators.¹ We therefore also check that the time-step of 1 fs employed gives acceptable value of λ for Drude masses of $0.4 \leq m_D/\text{amu} \leq 5$ in our simulations, as shown in Fig. S5(b). Here, all these simulations belong to the weak-coupling regimes.

Further analysis by extracting the static component, quantified by $\langle \mathcal{F}^2 \rangle$, and the dynamical component, quantified by τ_F , of the friction is shown in Fig. S6. This reveals that although values of λ converge for $m_D \lesssim 2$ amu for a time-step of 1 fs, the values of $\langle \mathcal{F}^2 \rangle$ and τ_F diverges for these small masses. Therefore, in the main article, $\langle \mathcal{F}^2 \rangle$ and τ_F for $m_D \lesssim 2$ amu cases are computed from simulations using a time-step of 0.1 fs.

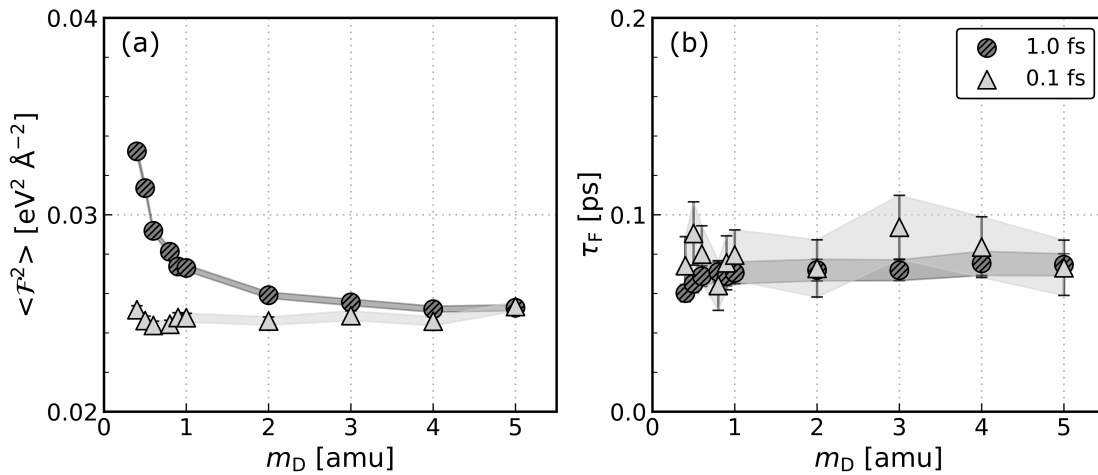


Figure S6. **Sensitivity of the static and dynamical components of friction to time-step.** Variation of (a) the mean squared force $\langle \mathcal{F}^2 \rangle$ and (b) the force decorrelation time τ_F for simulations with Drude masses $0.4 \leq m_D/\text{amu} \leq 5$ using a time-step of 0.1 and 1 fs.

S3.5. Thermostats

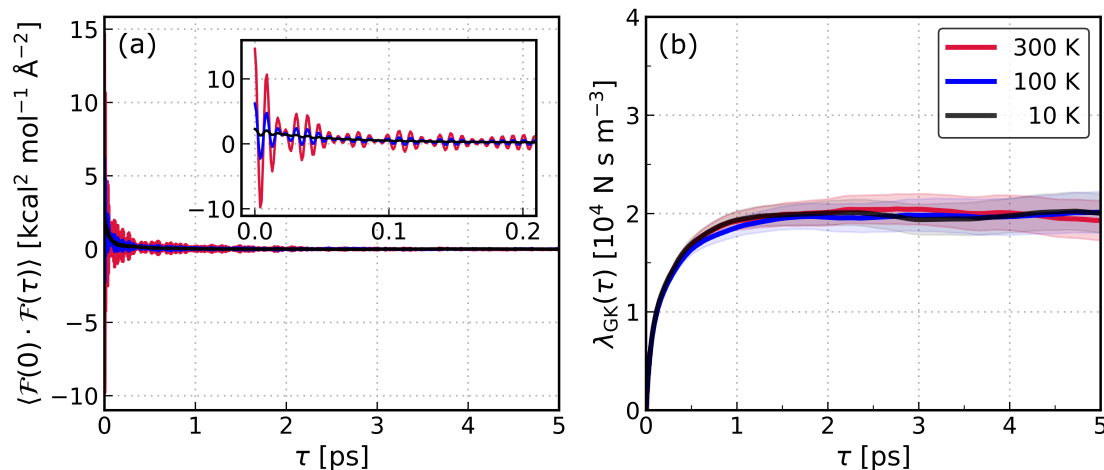


Figure S7. **Sensitivity of friction coefficient to the temperature of the Drude particles.** (a) The force autocorrelation function for simulations with $m_D = 1$ amu where the Drude particles are kept at $T_{\text{sol}} = 10, 100, 300$ K. The inset shows clearer the oscillations at short times. (b) The convergence of λ_{GK} for the three cases where statistical errors (shaded area) are obtained from block-averaging.

Ordinarily, in simulations of polarizable systems using the classical Drude oscillator model, the temperature of the Drude particles is often kept low^{1,3,28} to minimize energy exchange between the nuclear and Drude motion. In this work, we found numerical instabilities in simulations with low T_{sol} for $m_D \gtrsim 10$ amu. Therefore, for all results presented in this work, we used two separate thermostats to keep the temperatures of the water, T_{wat} , and the Drude particles, T_{sol} , both at 300 K. We carried out simulations with $m_D = 1$ amu (the weak-coupling regime) using different values for $T_{\text{sol}} = 10, 100$ and 300 K. As shown in Fig. S7, while the force autocorrelation function shows oscillations of greater magnitude at higher T_{sol} , its integral and therefore the friction coefficient is not significantly affected.

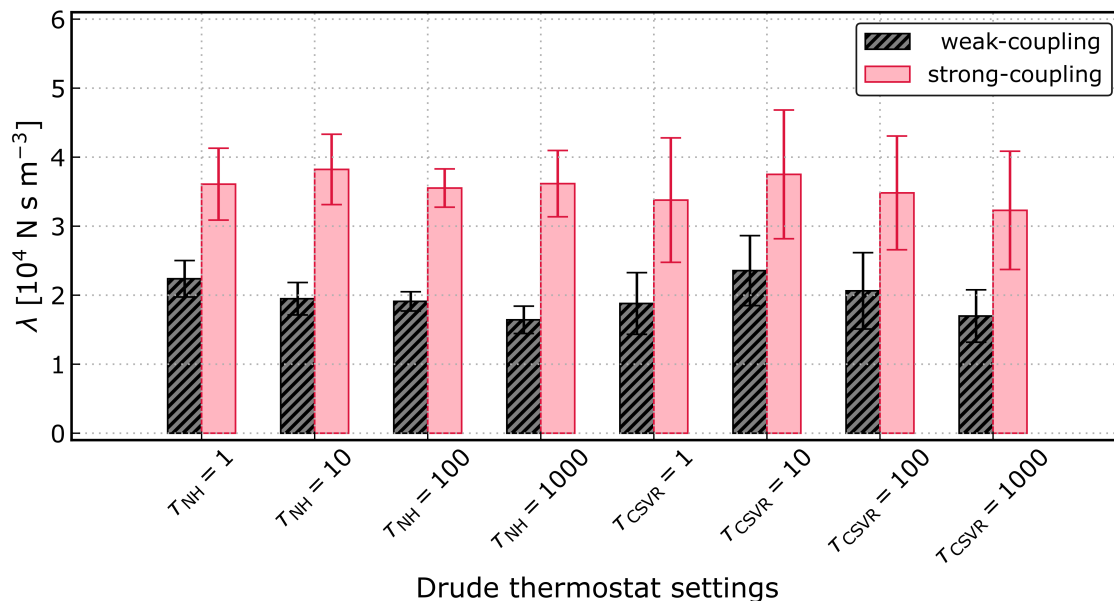


Figure S8. **Sensitivity of friction coefficient to thermostat settings for Drude particles.** The values of the damping time constant of the thermostat (τ_{NH} for the Nosé-Hoover thermostat and τ_{CSVR} for the CSVR thermostat) for the Drude particles are given in fs. Statistical errors are obtained from block-averaging.

We also test the sensitivity of the friction coefficient to the thermostat settings used to maintain the temperature of the Drude particles. In Fig. S8, we show that the friction coefficients agree well for different damping times of the Nosé–Hoover thermostat for the Drude particles $\tau_{\text{NH}} = 1, 10, 100, 1000$ fs in both the weak-coupling and strong-coupling regimes. Equivalent results were also obtained with the canonical sampling through velocity rescaling (CSVR) thermostat.²⁹

S3.6. Liquid film thickness

Simulations for systems with varying thickness of the water film were performed to test the convergence of the friction coefficient. In Fig. S9(a), we show the planar average mass density profiles for the liquid–solid system with a water film of thickness $\approx 7, 17, 27, 37$ and 47 Å. The thickness is determined by the height from the positions of the carbon atoms in the sheet to where the water density at the liquid–vapour interface is equal to 0.5 g cm^{-3} . In Fig. S9(b), we show how the extracted friction coefficient changes with the water film thickness. A water film with thickness $\gtrsim 17$ Å is required to have a region with bulk mass density and a converged friction coefficient. Therefore, employing a thickness of ≈ 37 Å for simulations of our main results is justified.

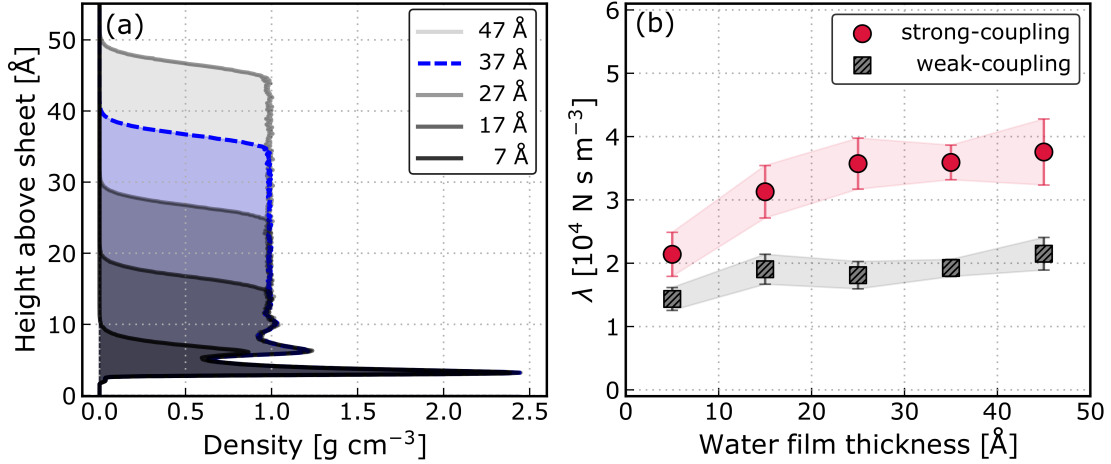


Figure S9. **Sensitivity of friction to simulation time to the liquid film thickness.** (a) The planar density profile of different film thicknesses above the flat solid sheet is shown for different water film thicknesses (indicated in the legend). In the main article, we use a thickness of ≈ 37 Å, as indicated by the dashed blue line. (b) The sensitivity of friction to the liquid thickness. Statistical errors are obtained from block-averaging.

S3.7. Electrostatic boundary conditions

For simulations presented in the main article, we treated electrostatics by applying the conventional three-dimensional Ewald summation (EW3D) technique.³⁰ This method is commonly employed in simulations of different interfacial systems.^{23,31,32} To test the influence of this choice to the friction coefficient, we performed additional simulations with hybrid boundary conditions in which the Ewald summation is applied to the x and y directions while the electric displacement field in the z direction is set to zero ($D_z = 0$). This is done using the finite field approach^{33–35} and such hybrid boundary conditions have been shown³³ to be formally equivalent to the Yeh–Berkowitz correction³⁶ that decouples the electrostatic interactions between a slab of material and its periodic images. We found good agreement for the friction coefficients of both the weak-coupling and strong-coupling regimes between the EW3D and the $D_z = 0$ methods, as shown in Fig. S10.

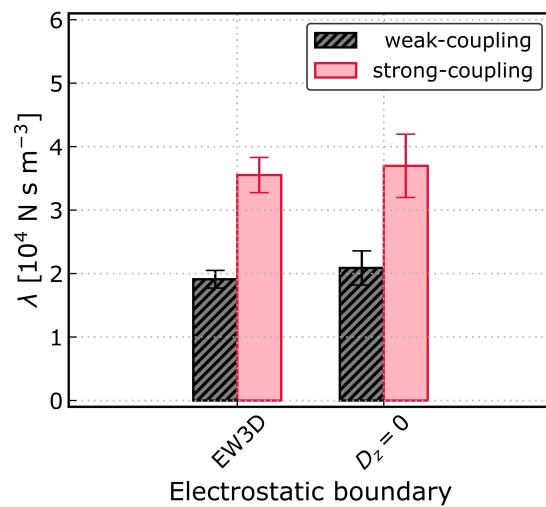


Figure S10. **Sensitivity of friction coefficient to electrostatic boundary conditions.** The friction coefficients in the weak-coupling and strong-coupling agree well for simulations employing the EW3D method and the $D_z = 0$ method. Statistical errors are obtained from block-averaging.

S4. COUPLING OF CHARGE DENSITIES

In this section, we present further analyses of the charge density power spectra of the solid and the liquid in support of the conclusions made on the separation into the weak-coupling and strong-coupling regimes in the main article.

S4.1. Charge densities in the absence of water

As in the main article, we first focus on the charge density of the solid, characterized by $S_{\text{sol}}(q, \omega)$, for simulations of a carbon sheet with Drude particles of mass $m_D = 10^3$ amu in the absence of water molecules. The frequency of oscillation for a single Drude oscillator in this case is given as $\omega_D = (k_D/m_D)^{1/2} = 3.26$ THz. All other simulation settings are kept the same as described in Sec. S1.

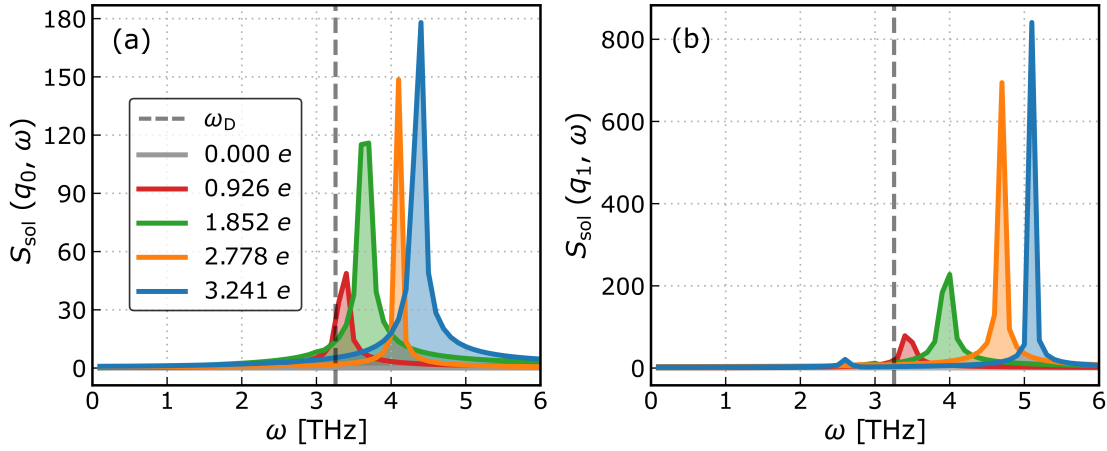


Figure S11. **Solid charge density in the absence of water.** The solid charge density spectrum $S_{\text{sol}}(q, \omega)$ of a carbon sheet with Drude particles of mass $m_D = 10^3$ amu in the absence of water is shown for different values of Q_D (indicated in the legend) at wavevectors (a) q_0 and (b) q_1 . The value of ω_D is marked with a dashed vertical line.

In Fig. S11, we show the variation of $S_{\text{sol}}(q_0, \omega)$ and $S_{\text{sol}}(q_1, \omega)$ as the charges of the Drude particles (and the core carbon atoms) are changed to $Q_D/e = 0, 0.926, 1.852, 2.778$ and 3.241 , where $q_0 = 2\pi/L_x \approx 0.25 \text{ \AA}^{-1}$, $q_1 = 4\pi/L_x \approx 0.49 \text{ \AA}^{-1}$ and e denotes the elementary charge. When $Q_D = 0$, there is no charge density in the solid so $S_{\text{sol}}(q, \omega) = 0$ and the graphene can be considered as a set of independent harmonic oscillators oscillating with frequency $\omega_0 = \omega_D$. As Q_D is increased, $S_{\text{sol}}(q_0, \omega)$ starts to exhibit a dominant peak with increasing intensity, which is in line with an increase in charge density in the system. The frequency of this peak at ω_0 gradually increases away from ω_D , indicating that the Drude oscillators are coupled with one another through their electrostatic interactions. The shift in frequency of the mode with highest intensity due to these interaction is increased for $S_{\text{sol}}(q_1, \omega)$. For $Q_D = 1.852e$ which we used in the simulations presented in the main article, $\omega_0 = 3.49$ THz. As $\omega_0 \approx \omega_D$, it is appropriate to consider the graphene sheet in this case to be a set of weakly coupled harmonic oscillators.

S4.2. Charge densities in the presence of water

In Fig. S12(a), the solid charge density spectra, $S_{\text{sol}}(q_0, \omega)$, are shown for simulations of the liquid-solid interface with various values of $m_D/\text{amu} = 1, 2, 5, 20, 50, 200, 1000$ and 5000 . The changes of the solid spectra going from in the absence to in the presence of water indicate dissipation in the solid due to coupling to the water charge density. These include the appearance of a broad feature at the low frequency end where the Debye peak in liquid water lies, common to all interfaces simulated with different values of m_D . While the peak with the highest intensity remains at $\omega = \omega_0 \approx \omega_D$ for all cases, it begins to broaden and decrease in height more significantly for cases in the strong-coupling regime.

In Fig. S12(b), we show only a single spectrum for the charge density of water since there are little to no changes upon changing m_D . We highlight the peak responsible for the librational motion of water

molecules, since this is at the frequency separating the weak-coupling regime and the strong-coupling regime as discussed in the main article.

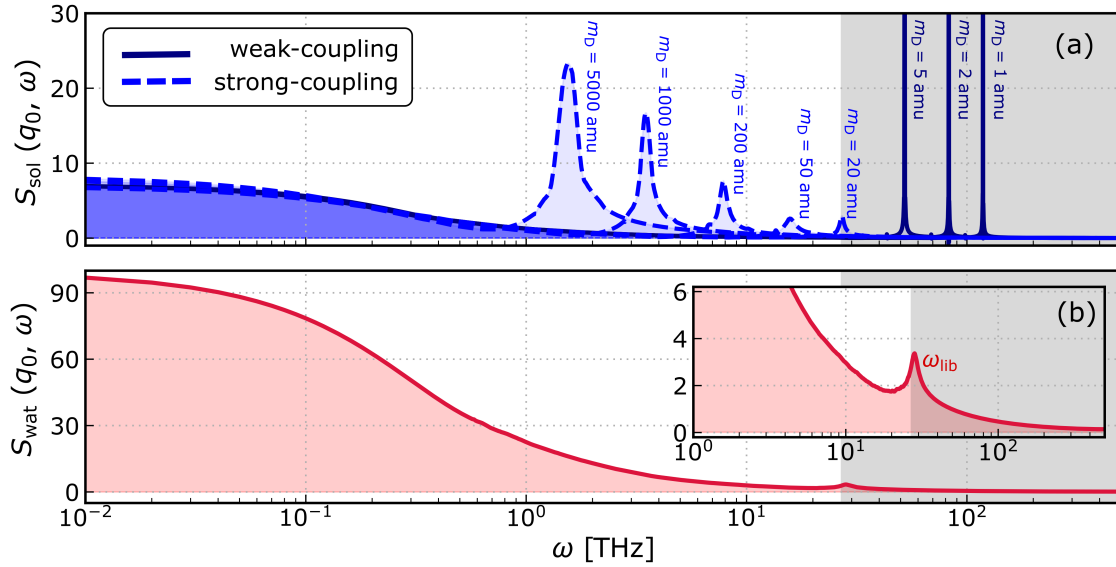


Figure S12. **Solid and water charge density spectra in the presence of water.** (a) $S_{\text{sol}}(q_0, \omega)$ for simulations of the liquid–solid interface with various values of m_D are plotted on top of each other. All spectra exhibit a broad feature at low frequency. Spectra belonging in the weak-coupling regime where the highest intensity peaked at ω_0 is not significantly damped are indicated by solid lines. Spectra belonging in the strong-coupling regime where peaked at ω_0 is significantly damped are indicated by dashed lines (b) $S_{\text{wat}}(q_0, \omega)$ for all cases show the same features: a small peak at ≈ 20 THz for the librational motion (see inset) and the broad peak at low frequency (the “Debye” peak).

S4.3. Force spectra

To further illustrate the change from the weak-coupling to the strong-coupling regime, we also computed the spectrum of the lateral force defined as

$$S_F(\omega) = \int_{-\infty}^{+\infty} dt \langle \mathcal{F}(0) \cdot \mathcal{F}(t) \rangle e^{i\omega t}. \quad (\text{S21})$$

We show $S_F(\omega)$ for simulations with Drude masses used the previous subsection in conjunction with the Green–Kubo friction $\lambda_{\text{GK}}(\tau)$ in Fig. S13. For cases belonging to the weak-coupling regime ($m_D/\text{amu} = 1, 2, \text{ and } 5$), $S_F(\omega)$ shows a peak due to the solid charge density at $\omega \approx \omega_0$ determined from $S_{\text{sol}}(q_0, \omega)$, and a broad feature at low ω from the water charge density. As m_D is increased, the peak due to the solid starts to merge with the water broad feature and increase in intensity. This can be linked to the behavior of $\lambda_{\text{GK}}(\tau)$ in the strong-coupling regime ($m_D/\text{amu} = 20, 50, 200, 1000$ and 5000): the increase in $S_F(\omega = \omega_0)$ is responsible for stronger oscillations in $\lambda_{\text{GK}}(\tau)$ at shorter times ($\tau < \tau_F$) while the increase in $S_F(\omega \lesssim \omega_0)$ is responsible for a higher plateau value at longer times ($\tau \geq \tau_F$).

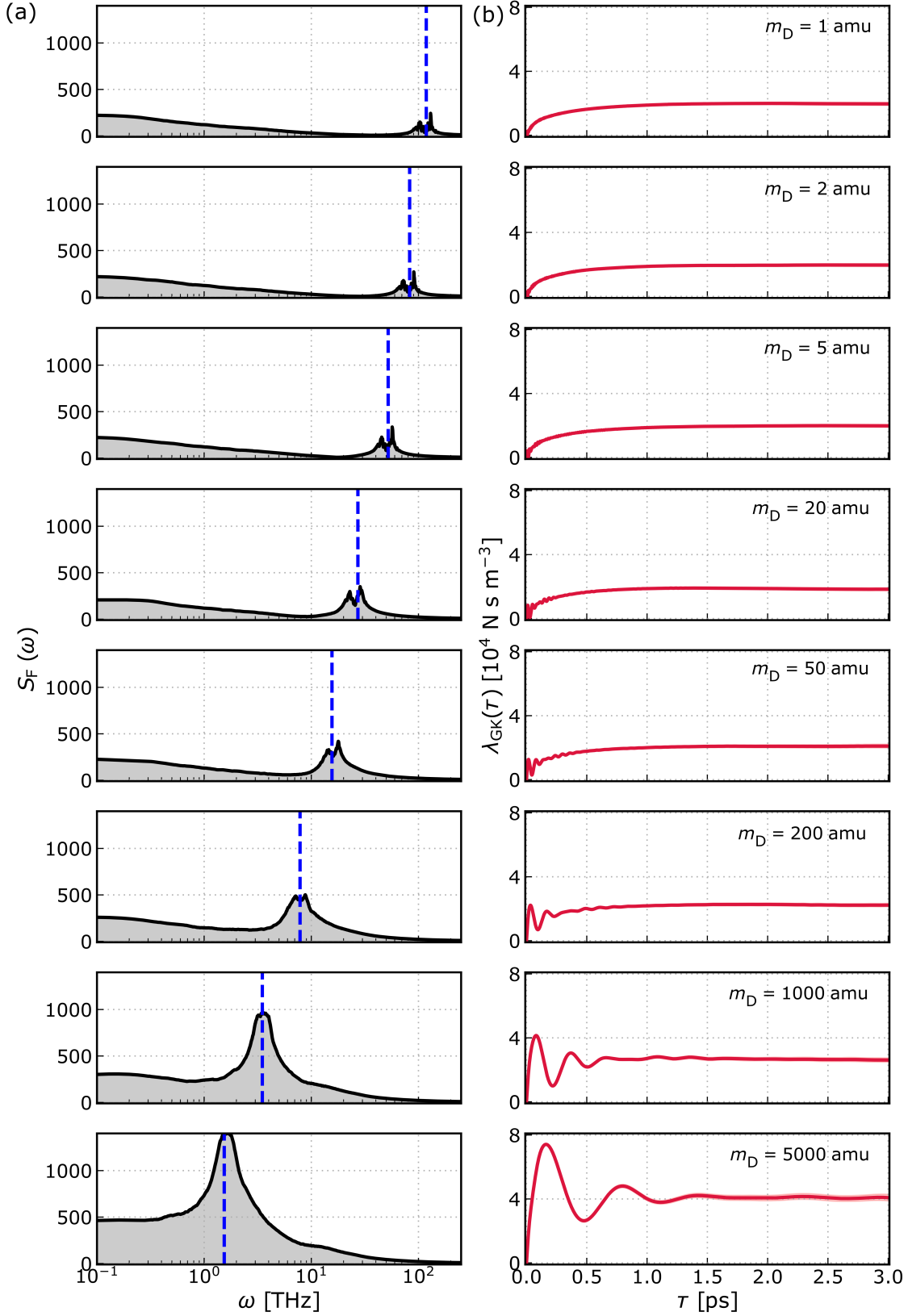


Figure S13. **Lateral force spectra.** (a) $S_F(\omega)$ for simulations with different m_D . The value of ω_0 extracted from $S_{sol}(q_0, \omega)$, marked as a dashed blue line, match with the frequency of the peak in $S_F(\omega)$ due to solid charge density contribution. This peak shows higher intensity as we move from the weak-coupling regime ($m_D < 20$ amu) to the strong-coupling regime ($m_D \geq 20$ amu). (b) This change manifests in $\lambda_{GK}(\tau)$ as the appearance of small oscillations at short τ and the increase in the plateau value at longer τ .

S5. SENSITIVITY OF THE DEPENDENCE OF FRICTION ON SOLID CHARGE DENSITY FREQUENCY

For the simulations presented in the main article, we fixed $Q_D = 1.852 e$ and $k_D = 1000 \text{ kcal mol}^{-1} \text{ \AA}^{-2}$ for the Drude oscillators, which have been parameterized by Misra and Blanckstein to recover the polarizability tensor of a periodic graphene lattice.¹⁴ In principle, Q_D and k_D both control the solid charge density and changing their values will affect the coupling between the solid and the liquid charge densities, and therefore the friction. Here we will present a check for the sensitivity of the dependence of friction on solid charge density frequency upon changing to different values for each of these parameters.

S5.1. Varying the Drude charge Q_D

We performed two additional sets of simulations of the liquid–solid interface with $Q_D = 0$ and $0.926 e$ while keeping $k_D = 1000 \text{ kcal mol}^{-1} \text{ \AA}^{-2}$ for Drude masses in the range $1 \lesssim m_D/\text{amu} \lesssim 10^7$ while other aspects of the simulations are kept the same. In the main article, we show the dependence of the friction on the frequency of the solid charge density by plotting λ against ω_0 . Based on the discussion in Sec. S4, we can approximate the solid charge density as $\omega_0 \approx \omega_D$ instead. Therefore, for convenience, in these additional analyses, λ is plotted against ω_D as shown in Fig. S14. The relationship mapped out for $Q_D = 1.852 e$ is essentially unchanged compared to the one presented in Fig. 2(a) in the main article.

For $Q_D = 0$, there is no charge density in the solid, i.e. $\tilde{n}_{\text{sol}}(\mathbf{q}, \omega) = 0$, so the only contribution to friction is from the surface roughness. Therefore the friction remains constant with ω_D at $\lambda \approx 1.7 \times 10^4 \text{ N s m}^{-3}$. Increasing Q_D to 0.926 and $1.852 e$ slightly increases the surface roughness contribution to friction, as seen from the flattening in the weak-coupling regime. Meanwhile, the contribution to friction from charge density coupling increases much more significantly in the strong-coupling regime for higher values of Q_D . This behavior supports the fact that the increase in friction at the low frequency end is indeed due to coupling of charge density between the solid and the liquid and larger charge density in the solid will couple more strongly with the liquid, resulting a larger increase in friction the strong-coupling regime.

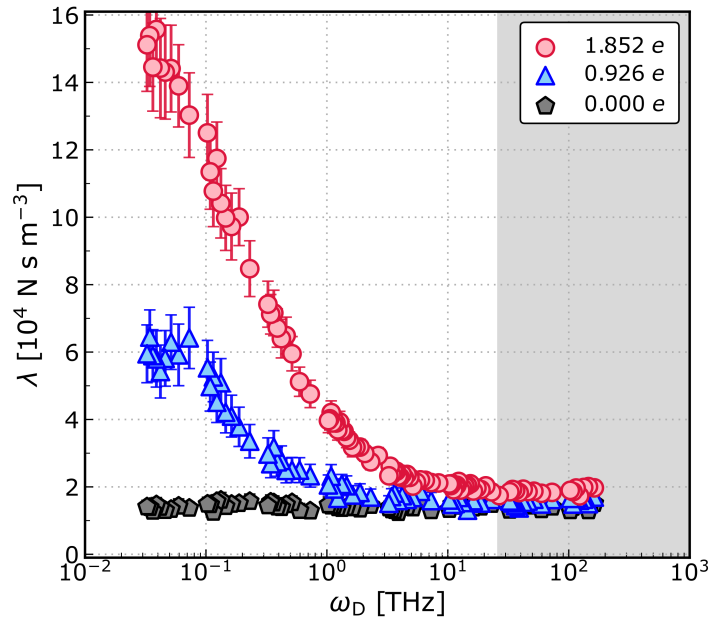


Figure S14. **Dependence of friction on solid charge density frequency for different Drude charges.** Values of Q_D are indicated in the legend and $k_D = 1000 \text{ kcal mol}^{-1} \text{ \AA}^{-2}$ in all cases. The weak-coupling and strong-coupling regimes are not shaded and shaded grey, respectively. For simulations with $Q_D = 0$, λ remains constant with ω_D . For simulations with $Q_D = 0.926$ and $1.852 e$, λ increases as ω_D is decreased in the strong-coupling regime.

S5.2. Varying the force constant k_D

Here, we performed two additional sets of simulations of the liquid–solid interface with $k_D = 600$ and $1000 \text{ kcal mol}^{-1} \text{ \AA}^{-2}$ while keeping $Q_D = 1.852 e$, also for Drude masses in the range $1 \lesssim m_D/\text{amu} \lesssim 10^7$, while other aspects of the simulations are kept the same.

Again, since the solid charge density is changed when k_D is varied, differences in the absolute values of λ are expected and indeed observed, as shown in Fig. S15. According to Eq. S6, a decrease in k_D means that the atom modeled by the Drude oscillator becomes less polarizable. Therefore, the friction contribution due to the surface roughness is higher for lower values of k_D but the differences in the λ in the weak-coupling regime are relatively small. The contribution to friction from charge density coupling is observed to be more strongly affected since λ increases much more sharply for lower k_D as ω_D is decreased in the strong-coupling regime. The important thing to stress is that this increase of λ due to charge density coupling in all cases occur once $\omega_D \lesssim \omega_{\text{lib}}$, supporting the separation into the weak-coupling and strong-coupling regimes in the main article.

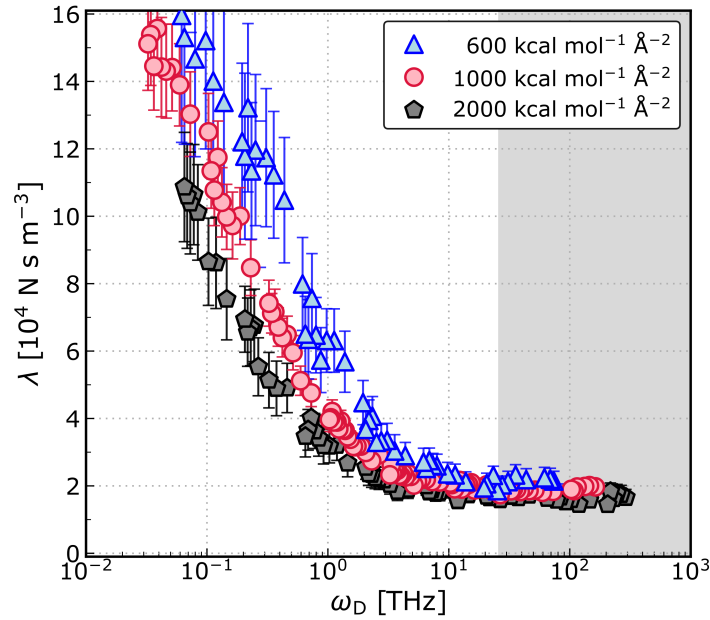


Figure S15. **Dependence of friction on solid charge density frequency for different harmonic force constant.** Values of k_D are indicated in the legend and $Q_D = 1.852 e$ in all cases. The weak-coupling and strong-coupling regimes are not shaded and shaded grey, respectively. For all cases, λ increases once $\omega_D \lesssim \omega_{\text{lib}}$ in the strong-coupling regime.

S6. ADDITIONAL PROPERTIES OF THE INTERFACE

S6.1. Static properties

For static properties in the liquid, we analyse the density profiles of the water along the surface normal. These are identical for the weak-coupling and the strong-coupling cases, as shown in Fig. S16(a). In the solid, the magnitude of the dipole moment of a Drude oscillator can be obtained from $\mu_D = Q_D d$ where d is the distance of the Drude particle from the core atom. We look at its probability distribution $p(\mu_D)$ for both cases, as shown in Fig. S16(b). In both cases, $p(\mu_D)$ is identical, reinforcing that the interatomic potential, and therefore all static equilibrium properties of the interface are not affected when m_D is varied.

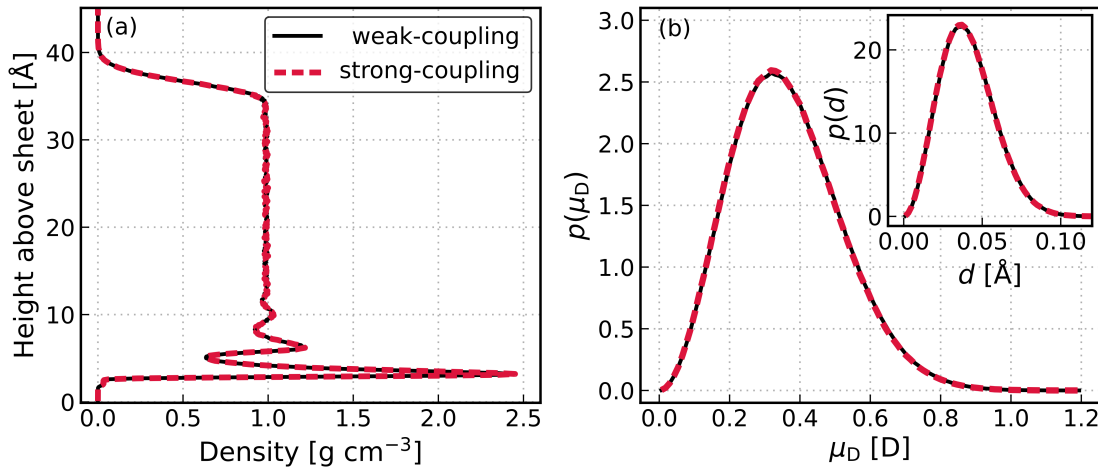


Figure S16. **Static equilibrium properties.** (a) The planar mass density profiles of the water are identical for the weak-coupling and the strong-coupling cases, showing a maximum density of $\approx 2.5 \text{ g cm}^{-3}$ and is at a height $\approx 3.2 \text{ Å}$ for the contact layer of water. (b) The probability distributions of the dipole moment magnitude of a Drude oscillator $p(\mu_D)$ in the solid are also identical for both cases, with the average of the distribution at $\langle \mu_D \rangle \approx 0.36 \text{ D}$. The inset shows the distribution of the distance between the Drude particles and their cores $p(d)$.

To link these observations to the unchanged static component of the friction coefficient described in the main article, we also look at the corrugation of the free energy surface (FES) experienced by the water molecules. Following previous work,^{22,37,38} the two-dimensional FES of species i is given by

$$\Delta G_i(x, y) = -k_B T \ln[p_i(x, y)], \quad (\text{S22})$$

where $p_i(x, y)$ is the normalized two-dimensional probability of finding species i in the contact layer at point (x, y) . For every saved configuration, we define the contact layer as consist of water molecules with height above the sheet $\leq 5 \text{ Å}$, where the first minimum in the density profile is. After computing both $p_O(x, y)$ and $p_H(x, y)$ and averaging onto a unit cell in the solid, we obtained the oxygen-based and hydrogen-based FESs. To ensure each surface is independent of noise, a Savitzky-Golay filter²⁵ was applied. The corrugation of each FES, ΔG_O and ΔG_H , can be quantified by taking the highest free energy present in the FES. As shown in Fig. S17, the water molecules experience the same oxygen-based and hydrogen-based FES at the liquid-solid interface in the weak-coupling and the strong-coupling regimes. Since corrugation is much more pronounced in the oxygen-based FES, we show ΔG_O as an approximation of the total corrugation in the main article.

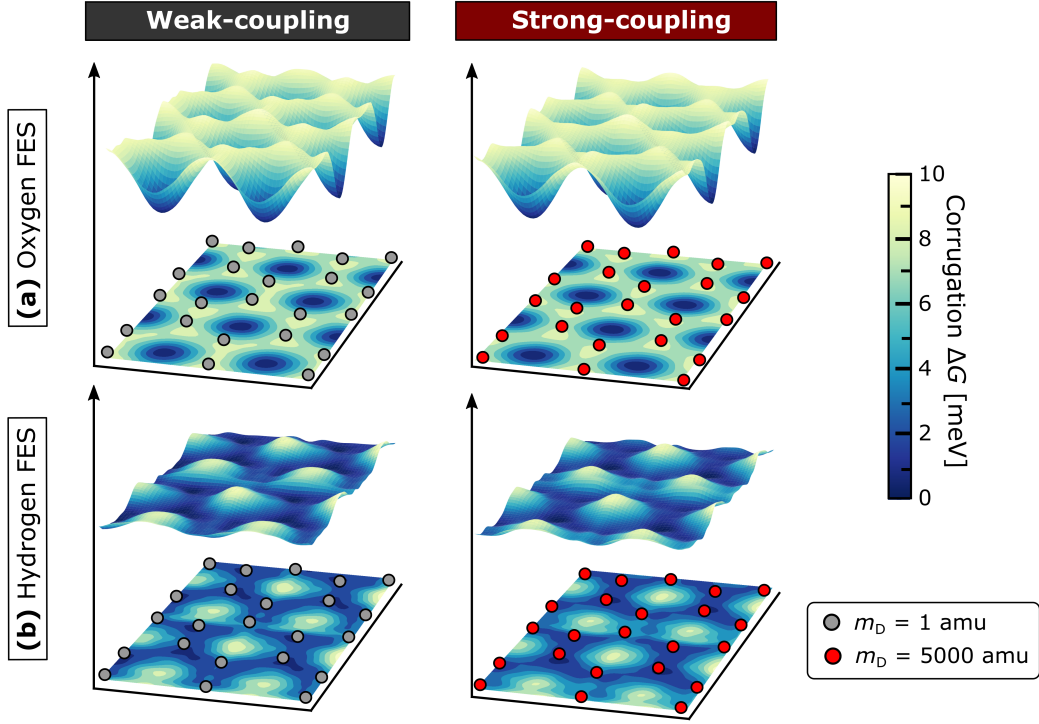


Figure S17. **Free energy surface corrugation** (a) The oxygen-based FES shows that oxygen atoms preferentially sit on hollow sites in the middle of the hexagon rings in graphene. (b) The hydrogen-based FES, which is less corrugated than the oxygen-based FES, shows that hydrogen atoms preferentially sit on carbon sites. The solid atoms are represented by the markers in the projection where the core atom in the Drude oscillator with $m_D = 1$ amu is in grey and $m_D = 5000$ amu in red. Both FESs show identical level of corrugation in the weak-coupling and strong-coupling cases.

S6.2. Dynamical properties

In addition to the charge density relaxation, we also explored other dynamical properties of water including its orientational relaxation and hydrogen-bonding relaxation. The orientational dynamics of water molecules in the liquid is examined, following Yeh and Mou,³⁹ via the second-order rotational autocorrelation function, defined as

$$C_{\text{rot}}(\tau) = \langle P_2[\mathbf{u}(0) \cdot \mathbf{u}(\tau)] \rangle, \quad (\text{S23})$$

where $\mathbf{u}(\tau)$ is the unit vector along the water molecular dipole at time τ and $P_2(x)$ denotes the second Legendre Polynomial. The hydrogen-bond relaxation is examined via the autocorrelation function of the presence of a hydrogen bond, defined as

$$C_{\text{hb}}(\tau) = \frac{\langle h(0) \cdot h(\tau) \rangle}{\langle h^2 \rangle}, \quad (\text{S24})$$

where $h(\tau) = 1$ if there is a hydrogen bond between a pair of water molecules at time τ and $h(\tau) = 0$ otherwise. Two water molecules are considered to be hydrogen-bonded according to geometric criteria from Luzar and Chandler.⁴⁰

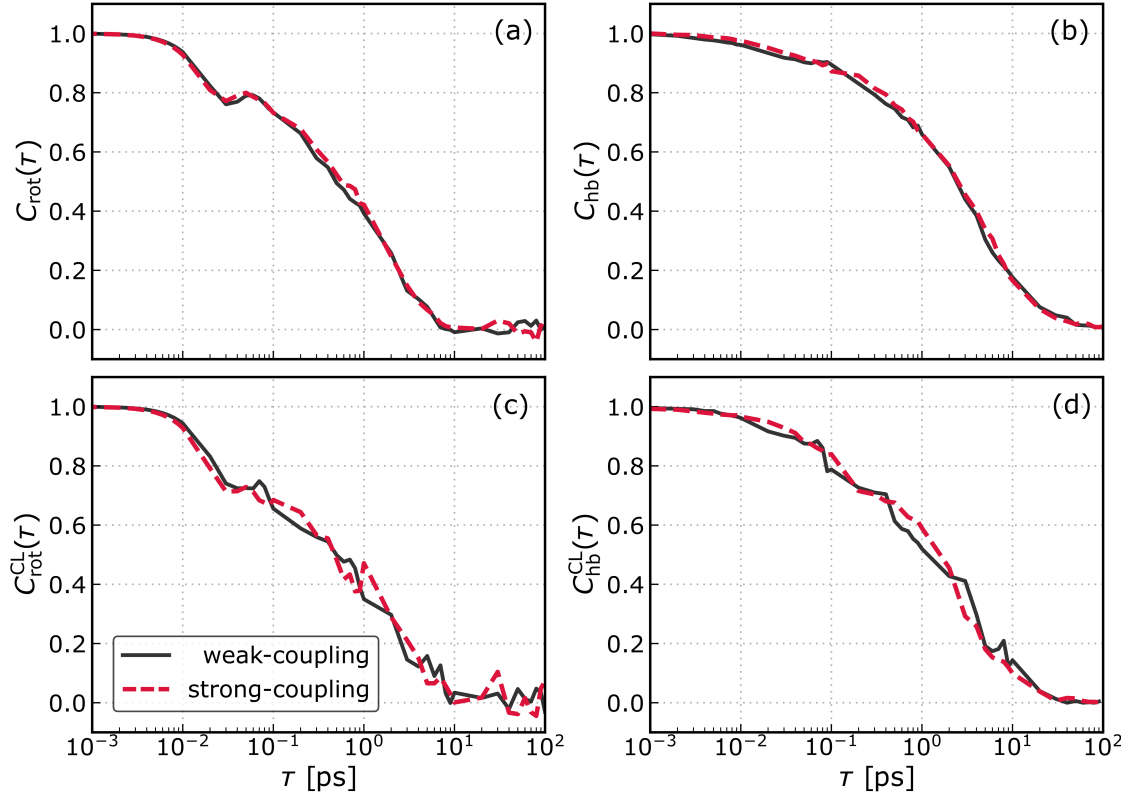


Figure S18. **Dynamical properties of water.** The rotational autocorrelation (a and c) and the hydrogen-bonding autocorrelation (b and d) are both barely affected between the weak-coupling and the strong-coupling regimes. The functions are computed for the whole water film (a and b) and just the contact layer (c and d).

From Figs. S18(a) and (b), we see little differences between the weak-coupling and strong-coupling cases for both $C_{\text{rot}}(\tau)$ and $C_{\text{hb}}(\tau)$ computed for the whole water film. These observations still hold when we look at $C_{\text{rot}}^{\text{CL}}(\tau)$ and $C_{\text{hb}}^{\text{CL}}(\tau)$, in Figs. S18(c) and (d), where superscript CL denotes that the autocorrelation functions are defined for just the contact layer (defined as the layer from the carbon sheet up to the first minimum of the water density profile). This supports our conclusion that the increase in friction due to charge density coupling has little impact on the behavior of the liquid.

REFERENCES

- ¹G. Lamoureux and B. Roux, "Modeling induced polarization with classical Drude oscillators: Theory and molecular dynamics simulation algorithm," *The Journal of Chemical Physics* **119**, 3025–3039 (2003).
- ²B. T. Thole, "Molecular polarizabilities calculated with a modified dipole interaction," *Chemical Physics* **59**, 341–350 (1981).
- ³C. Schröder and O. Steinhauser, "Simulating polarizable molecular ionic liquids with Drude oscillators," *The Journal of Chemical Physics* **133**, 154511 (2010).
- ⁴S. Y. Noskov, G. Lamoureux, and B. Roux, "Molecular dynamics study of hydration in ethanolwater mixtures using a polarizable force field," *The Journal of Physical Chemistry B* **109**, 6705–6713 (2005).
- ⁵G. Lamoureux, E. Harder, I. V. Vorobyov, B. Roux, and A. D. MacKerell, "A polarizable model of water for molecular dynamics simulations of biomolecules," *Chemical Physics Letters* **418**, 245–249 (2006).
- ⁶J.-L. Barrat and L. Bocquet, "Influence of wetting properties on hydrodynamic boundary conditions at a fluid/solid interface," *Faraday Discuss.* **112**, 119–128 (1999).
- ⁷K. Falk, F. Sedlmeier, L. Joly, R. R. Netz, and L. Bocquet, "Ultralow liquid/solid friction in carbon nanotubes: Comprehensive theory for alcohols, alkanes, OMCTS, and water," *Langmuir* **28**, 14261–14272 (2012).
- ⁸S. Plimpton, "Fast parallel algorithms for short-range molecular dynamics," *Journal of Computational Physics* **117**, 1–19 (1995).
- ⁹A. P. Thompson, H. M. Aktulga, R. Berger, D. S. Bolintineanu, W. M. Brown, P. S. Crozier, P. J. in 't Veld, A. Kohlmeyer, S. G. Moore, T. D. Nguyen, R. Shan, M. J. Stevens, J. Tranchida, C. Trott, and S. J. Plimpton, "LAMMPS - a flexible simulation tool for particle-based materials modeling at the atomic, meso, and continuum scales," *Computer Physics Communications* **271**, 108171 (2022).
- ¹⁰H. J. C. Berendsen, J. R. Grigera, and T. P. Straatsma, "The missing term in effective pair potentials," *The Journal of Physical Chemistry* **91**, 6269–6271 (1987).
- ¹¹H. C. Andersen, "Rattle: A "velocity" version of the shake algorithm for molecular dynamics calculations," *Journal of Computational Physics* **52**, 24–34 (1983).
- ¹²T. Werder, J. H. Walther, R. L. Jaffe, T. Halicioglu, and P. Koumoutsakos, "On the water-carbon interaction for use in molecular dynamics simulations of graphite and carbon nanotubes," *The Journal of Physical Chemistry B* **107**, 1345–1352 (2003).
- ¹³A. Dequidt, J. Devémy, and A. A. H. Prádua, "Thermalized Drude oscillators with the LAMMPS molecular dynamics simulator," *Journal of Chemical Information and Modeling* **56**, 260–268 (2016).
- ¹⁴R. P. Misra and D. Blankschtein, "Insights on the role of many-body polarization effects in the wetting of graphitic surfaces by water," *The Journal of Physical Chemistry C* **121**, 28166–28179 (2017).
- ¹⁵R. Hockney and J. Eastwood, *Computer Simulation Using Particles* (Adam-Hilger, 1988).
- ¹⁶J. Kolafa and J. W. Perram, "Cutoff errors in the ewald summation formulae for point charge systems," *Molecular Simulation* **9**, 351–368 (1992).
- ¹⁷W. Shinoda, M. Shiga, and M. Mikami, "Rapid estimation of elastic constants by molecular dynamics simulation under constant stress," *Phys. Rev. B* **69**, 134103 (2004).
- ¹⁸M. E. Tuckerman, J. Alejandre, R. López-Rendón, A. L. Jochim, and G. J. Martyna, "A liouville-operator derived measure-preserving integrator for molecular dynamics simulations in the isothermal-isobaric ensemble," *Journal of Physics A: Mathematical and General* **39**, 5629–5651 (2006).
- ¹⁹L. Bocquet and J.-L. Barrat, "Hydrodynamic boundary conditions, correlation functions, and kubo relations for confined fluids," *Phys. Rev. E* **49**, 3079–3092 (1994).
- ²⁰L. Bocquet, J.-P. Hansen, and J. Piasecki, "Friction tensor for a pair of brownian particles: Spurious finite-size effects and molecular dynamics estimates," *Journal of Statistical Physics* **89**, 321–346 (1997).
- ²¹P. Español, J. A. de la Torre, and D. Duque-Zumajo, "Solution to the plateau problem in the Green-Kubo formula," *Phys. Rev. E* **99**, 022126 (2019).
- ²²G. Tocci, L. Joly, and A. Michaelides, "Friction of water on graphene and hexagonal boron nitride from ab initio methods: Very different slippage despite very similar interface structures," *Nano Letters* **14**, 6872–6877 (2014).
- ²³A. R. Poggioli and D. T. Limmer, "Distinct chemistries explain decoupling of slip and wettability in atomically smooth aqueous interfaces," *The Journal of Physical Chemistry Letters* **12**, 9060–9067 (2021).
- ²⁴H. Oga, Y. Yamaguchi, T. Omori, S. Merabia, and L. Joly, "Green-Kubo measurement of liquid-solid friction in finite-size systems," *The Journal of Chemical Physics* **151**, 054502 (2019).
- ²⁵A. Savitzky and M. J. E. Golay, "Smoothing and differentiation of data by simplified least squares procedures," *Analytical Chemistry* **36**, 1627–1639 (1964).
- ²⁶A. Seal and A. Govind Rajan, "Modulating water slip using atomic-scale defects: Friction on realistic hexagonal boron nitride surfaces," *Nano Letters* **21**, 8008–8016 (2021).
- ²⁷L. Joly, G. Tocci, S. Merabia, and A. Michaelides, "Strong coupling between nanofluidic transport and interfacial chemistry: How defect reactivity controls liquid-solid friction through hydrogen bonding," *The Journal of Physical Chemistry Letters* **7**, 1381–1386 (2016).
- ²⁸C. Rupakheti, G. Lamoureux, A. D. MacKerell, and B. Roux, "Statistical mechanics of polarizable force fields based on classical drude oscillators with dynamical propagation by the dual-thermostat extended lagrangian," *The Journal of Chemical Physics* **153**, 114108 (2020).
- ²⁹G. Bussi, D. Donadio, and M. Parrinello, "Canonical sampling through velocity rescaling," *The Journal of Chemical Physics* **126**, 014101 (2007).
- ³⁰J. C. Shelly, "Boundary condition effects in simulations of water confined between planar walls," *Molecular Physics* **88**, 385–398 (1996).
- ³¹J. Alejandre, D. J. Tildesley, and G. A. Chapela, "Molecular dynamics simulation of the orthobaric densities and surface tension of water," *The Journal of Chemical Physics* **102**, 4574–4583 (1995).
- ³²S. E. Feller, R. W. Pastor, A. Rojnuckarin, S. Bogusz, and B. R. Brooks, "Effect of electrostatic force truncation on interfacial and transport properties of water," *The Journal of Physical Chemistry* **100**, 17011–17020 (1996).
- ³³C. Zhang and M. Sprik, "Computing the dielectric constant of liquid water at constant dielectric displacement," *Phys. Rev. B* **93**, 144201 (2016).

- ³⁴C. Zhang and M. Sprik, “Finite field methods for the supercell modeling of charged insulator/electrolyte interfaces,” *Phys. Rev. B* **94**, 245309 (2016).
- ³⁵S. J. Cox and M. Sprik, “Finite field formalism for bulk electrolyte solutions,” *The Journal of Chemical Physics* **151**, 064506 (2019).
- ³⁶I.-C. Yeh and M. L. Berkowitz, “Ewald summation for systems with slab geometry,” *The Journal of Chemical Physics* **111**, 3155–3162 (1999).
- ³⁷G. Tocci, M. Bilichenko, L. Joly, and M. Iannuzzi, “Ab initio nanofluidics: disentangling the role of the energy landscape and of density correlations on liquid/solid friction,” *Nanoscale* **12**, 10994–11000 (2020).
- ³⁸F. L. Thiemann, C. Schran, P. Rowe, E. A. Müller, and A. Michaelides, “Water flow in single-wall nanotubes: Oxygen makes it slip, hydrogen makes it stick,” *ACS Nano* **16**, 10775–10782 (2022).
- ³⁹Y.-I. Yeh and C.-Y. Mou, “Orientational relaxation dynamics of liquid water studied by molecular dynamics simulation,” *The Journal of Physical Chemistry B* **103**, 3699–3705 (1999).
- ⁴⁰A. Luzar and D. Chandler, “Hydrogen-bond kinetics in liquid water,” *Nature* **379**, 55–57 (1996).